University of Southampton

Faculty of Engineering and Physical Sciences

Electronics and Computer Science

Micro-thermal Flow-rate Detection for Lab-on-a-chip Technologies

by

Jack J. Tyson

A project report submitted for the degree of

Bachelor of Engineering

April 2018

Abstract

Flow-rate detection forms an integral component of a wide variety of analysis systems. With the micro-scale advancements of such technologies this is an area of interest, particularly for fluid-based medical applications, in which many different form-factors employing a variety of different detection methods can be seen. In this paper, an investigation into the plausibility and implications behind the application of a new calorimetric-based thermal flow-rate sensor for micro-fluidic lab-on-a-chip devices was conducted. Several variants of the design were created to identify the combination of components and input parameters yielding the best performance. Passive sensors offered a power-efficient, noise and drift resistant solution, proving stable flow-rate detection could be achieved using electrode plates in-place of the common hot-wire techniques used widely at the time. This design could also be used in-conjunction with digital computation hardware for integrated analysis and reporting on-chip without the need for expensive external hardware.

Keywords: *lab-on-a-chip, micro-fluidics, micro-thermal, micro-sensors, flow-rate detection, electromagnetic heating*

Contents

List of Figures

List of Tables

List of Symbols

A	Area (m^2)
c_0	Molar concentration (mol/m^3)
c_L	Speed (m/s)
c_V	Flow-rate (μL/min)
C	Capacitance (F)
E	Electric field magnitude (V/m)
f	Frequency (Hz)
h	Heat transfer coefficient (W/m^2K)
H	Attenuation factor
j	Imaginary unit
k	Boltzmann constant (J/K)
L	Length (m)
M	Molar mass (mol/L)
N_A	Avogadro constant (mol^{-1})
p/P	AC/DC Power (W)
q	Electron charge (C)
Q	Heat energy (J)
R	Resistance (Ω)
T	Temperature (K)
u/U	AC/DC voltage
V	Volume (m^3)
X	Capacitive reactance (Ω)
Z	Impedance (Ω)
ϵ_0	Permittivity of free space (F/m)
ϵ_r	Relative permittivity
λ_D	Debye length (m)
ϕ	Phase shift (rad)
ω	Angular frequency (rad/s)

List of Abbreviations

BNC	**B**ayonet **N**eill–**C**oncelman
DMFB	**D**igital **m**icro-**f**luidic **b**iochip
EDL	**E**lectrical **d**ouble **l**ayer
LIA	**L**ock-**i**n **a**mplifier
LOC	**L**ab-**o**n-a-**c**hip
MEMS	**M**icro-**e**lectro**m**echanical **s**ystem
MFC	**M**icro-**f**luidic **c**hip
PBS	**P**hosphate-**b**uffered **s**aline
PCB	**P**rinted **c**ircuit **b**oard
PIC	**P**eripheral **i**nterface **c**ontroller
POCT	**P**oint-**o**f-**c**are **t**esting
PSD	**P**hase-**s**ensitive **d**etection
RMS	**R**oot **m**ean **s**quare
μTAS	**M**icro-**t**otal-**a**nalysis-**s**ystem

Chapter 1

Introduction

The ability to observe and analyse the flow of a gas or liquid within a medium of varying complexity has distinct applications ranging from the monitoring of fuel flow and quality through an internal combustion engine, to the sensitive observation and subsequent control of a clean-room environment operating under strict sterile conditions. The potential applications of such technologies have been further expanded into the realm of medical-orientated lab-on-a-chip devices to perform tasks, such as the precise detection and monitoring of various biological cells, as well as the screening of blood to gauge its properties and the presence of any potential pathogens. Medical devices and smarter diagnostics are becoming increasingly more crucial to both doctors and patients alike; an increasing number of potentially life-threatening conditions require far more unique solutions in order to detect, combat and eventually prevent entirely.

Flow-rate measurement, and subsequent control, plays a primary role in the operation of micro-fluidic medical technologies. Many designs for such systems have been developed, some employing the more common thermal-based detection methods, whilst others utilise solely electrical properties. In the case of thermal flow-rate sensors, thermal diffusion occurs along a thermal gradient from an area of higher temperature to that of a lower temperature. This process occurs throughout any type of media, whether it be a solid, liquid or gas. By analysing the diffusion pattern of a burst of heat energy, many useful properties of that medium can be identified. Many designs for micro-thermal flow-rate sensors have been submitted before that discussed in this account. However, many of these designs are undistinguished in that they rely too heavily on the properties of the fluid being monitored.

The motivation behind this project was the need to create an un-intrusive, low-powered and accurate flow-rate measurement device; criteria unfulfilled by the majority of designs readily available at the time of writing this account. Proposed here is a new design for a micro-thermal flow-rate sensor constructed within a LOC device to detect the flow-rate of saline accurately at flow-rates suitable for the technology. Electrode plates were utilised at the electrical-fluidic interface as opposed to the common hot-wire technology, where a wire would partially obstruct the fluid flow. Plates placed flush against the channel walls offer far less disturbance to any medium under forced or natural flow, helping to prevent turbulent flows that can affect measurement accuracy. By applying a voltage to an electrically conductive fluid using these electrodes, energy will be dissipated into the saline in the form of heat.

On top of this, the calorimetric flow-rate sensor principle was applied to the entire system; two sensors, one upstream from the heat energy dissipater, and the other downstream from it enabled a comparison between the two sides to be carried out. With temperature effecting the way a fluid behaves, be it electrically or physically, a direction-of-flow could be determined based on the direction the dissipated heat is 'carried' along.

By the end, the primary goal of this project was to be able to easily identify, categorise and analyse the flow-rate of saline through a micro-machined fluidic chip whilst detailing how the variation of temperature effects the properties of said fluid. As with this, going along with the design philosophy behind all LOC devices, an important area of consideration throughout was to develop a system capable of carrying-out these tasks without the need for vast, complex and expensive equipment; making this design be of great benefit across many disciplines such as Chemistry, Biology, Medicine and Engineering - all of which typically use such equipment to perform measurements at this scale.

Chapter 2

Literature Review

2.1 Micro-fluidics: A Retrospective

Over the years, strong advances in the field of microtechnology have paved the way to provide an increased interest into the process of micro-fabrication; continued refinement of fabrication methods has pioneered the development of advanced micro-machined flow sensors for the processing of both fluids and gasses in very small quantities. Micro-fluidic flow sensors can be one of two types; thermal or non-thermal [1]. In this account only thermal-based flow sensors for micro-fluidic applications were investigated.

The active interest in the further development of these particular sensors comes from a variety of distinct advantages over the alternatives; micro-machined thermal flow sensors have no moving parts, resulting in a largely simplified manufacturing process, considerable reduction in costs for both the producer and the consumer and a far lower risk of sensor failure [1]. On top of this, these sensors have a very low power consumption and can be far more sensitive given the appropriate electronic configuration [2]. Specific research into LOC devices has been driven by more recent advancements in micro-fabrication techniques [2, 3] as well as a greater interest into exploiting the benefits of micro-fluidics.

According to a book written by *Patrick Tabeling* [4], the first example of a micro-machined device surfaced in 1975 and held the form of a microscopic gas chromatography system created by *Stephen Clark Terry* [5], a Ph.D student at Stanford University. Tabeling states how this was a one-off creation that was out of its time, explaining that the industry had little need for such technologies, and as a result it was not ready to embrace its advantages. In contrast, the modern day equivalents of Terry's original device are used for a very wide range of applications ranging from precise environmental monitoring to more advanced gas chromatography systems [1].

This was not where development ended however, LOC or TAS devices offer great possibilities for Medicine, Biology and Chemistry [1, 2, 6–10] with applications in micro-coolant, micro-chemical analysis and fluid handling systems [6, 7, 9].

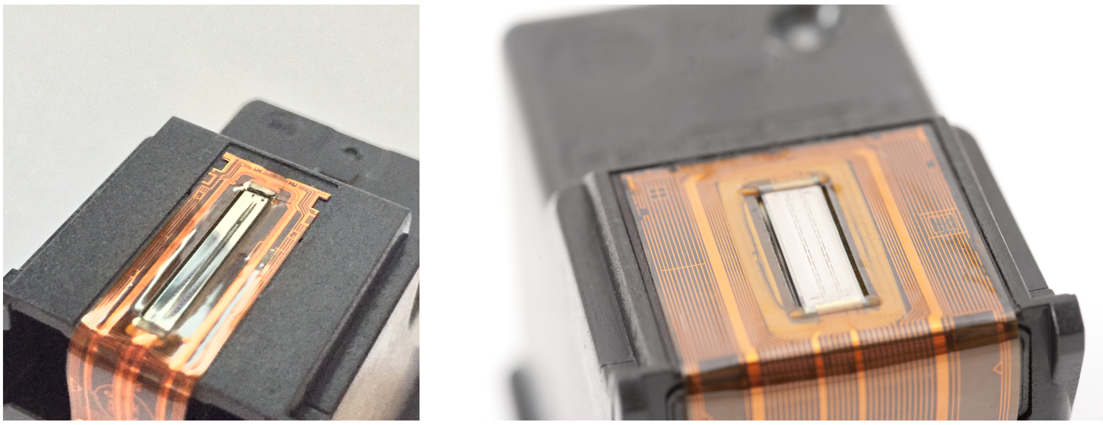

(a) (b)

Figure 2.1: Inkjet MEMS technology: A common-place micro-fluidic device is the inkjet print head. These devices apply their own MEMS topology in order to process very minute volumes of ink at any given time.

The abilities of LOC devices have also been extended into the area of tissue engineering [11]; characteristics of vital organs within the human body can be simulated in real-time and observed in great detail. This led to the creation of a second generation of LOC devices called DMFBs [3, 12, 13]. DMFBs are harder to manufacture, but offer even more precision over LOC technologies with dispensing applications processing fluid quantities from the microlitre (10^{-6}L) all the way down to the attolitre (10^{-18}L) [12, 13]. This opens the devices up to further, more advanced uses in the medical profession for parallel immunoassays, point-of-care diagnoses and pathogen detection [13].

2.2 Microtechnology and Microsensors

2.2.1 Point of Care Testing

Studies have shown how POCT devices are becoming increasingly more relevant in modern day medicine with an increasing range of applications being developed every year. Companies such as *Nova Biomedical*[1], *EKF Diagnostics*[2] and *Roche Diagnostics*[3] have each seen success from their active stance on the research and development of such technologies. The *NHS* have issued a report on the application of POCT HbA1c diagnostic systems to aid with the prevention of Diabetes [14], outlining how the widespread adoption of such a convenient technology had been repeatedly halted due to the concerns regarding its accuracy. This is not a one-off concern, where many other medical institutions have also described a lack of trust in such devices; where implemented, medical devices reporting concerning results often required a retest through more *"typical"* lab-based means [14].

However, as a result of their advantageous size, simplicity and reduced cost over

[1]`www.novabio.us`
[2]`www.ekfdiagnostics.com`
[3]`www.roche.co.uk`

a thorough and time-consuming analysis based in a laboratory, the drive for point of care systems has never been higher [15]. Essentially POCT is made up of three components; diagnosis, sample and analysis. A doctor would have made a diagnosis on the patient, obtain an appropriate medical sample from them based on that diagnosis, analyse that sample then issue the results back to the patient, all within a single appointment. Beneficial to both the patient and the doctor, ideally a treatment regime can be put in place after just a single visit, where both time and money can be saved on both sides. Active examples of POCT implementations include the previously discussed HbA1c testing kits, HIV salivary assays and Homocysteine testing kits.

2.2.2 Lab-on-a-chip

Formally referred to a μTAS, LOC is a broad-based, relatively generic term designated for devices capable of integrating lab-required tasks into a small footprint. These technologies have been actively developed due to their unmatched ability to negate the need for expensive and often robust equipment; minimising and simplifying much larger tasks remains the key driving point here. As a result of this, POCT comes under the broader-viewpoint of LOC technologies and shares in its unique benefits.

Though not the subject of this account, LOC devices can take a large array of purposes, form factors and complexities of their own. For instance, LOC systems can take the forms of micro-electro-mechanical, digital and/or analogue processing, chemical analysis and biological detection systems. New and innovative concepts and applications are not the sole focus for this area of technology. However, many traditional, flight-proven and occasionally outdated principles have been modernised and reapplied at the microscopic scale.

Advantages	Disadvantages
• Offers consistent, automated and accurate analysis fit-for-purpose. • Removes a large component of human error from specific processes. • Often disposable. • Power efficient. • Cheap to fabricate/purchase.	• Lab processes do not always scale-down correctly. • High initial set-up cost for fabrication processes. • Many LOC concepts have not yet reached the appropriate TRL[4] required for widespread adoption.

Table 2.1: Summarising the advantages and disadvantages of LOC technologies.

It has been shown that one of the most important applications of this technological

[4] *NASA* - The **T**echnology **R**eadiness **L**evel Directorate. `www.nasa.gov/directorates/heo/scan/engineering/technology/txt_accordion1.html`

form-factor comes in the form of microsensors, specifically for biological and chemical systems as described previously [16, 17]. Sensors of particular interest are those involving accurate particle and/or flow-rate detection [18], where many attempts to minimise existing methods, with varying success, have been attempted.

2.2.3 Thermal Flow-rate Sensor Principles

There are three fundamental types of micro-thermal flow-rate sensors embeddable on LOC devices [1]; hot-wire [19], calorimetric [20, 21] and time-of-flight [2]. Hot-wire anemometry is a process where a physical heating element is suspended within the medium in which the flow-rate is being identified. The element undergoes either free or forced convection depending on the nature of the medium that it is subject to. Heat is generated by passing a current through the element; obeying the law of power dissipation, any electrical resistance gives rise to a loss in energy and therefore a loss of current. The resistance of the element itself is dependant on temperature, which in turn is liable on the flow-rate of the gas or liquid surrounding it. From the combination of these variables, a sensor can be calibrated to detect a specific flow-rate by analysing the current passing through the heating element [22].

Time-of-flight flow-rate detection is another approach involving the detection of the heat transit time between a heater at position x, to a detector downstream at position y. In a previous joint research project [2], a pulse-modulated heat signal received at the detector, then cross-correlated with the electrical signal that created the original heat pulse, enabled a time offset to be established. From this offset a speed was easily determinable as the distance between x and y was known. This measurement technique has proven very accurate and can often detect far smaller flow-rates than other techniques [23] and has the added benefit of not being reliant on fluid properties to function correctly [2].

In comparison to others, calorimetric systems are far more easily configured to detect a fluid's velocity as opposed to just its speed [1]; this is made possible with the use of two sensor nodes, where the heater is situated between them. The calorimetric principle also boasts independence from the electrical conductivity, density and viscosity of the fluid-based medium it is analysing.

2.3 Micro-fluidic Chips

Micro-fluidic chips bridge the gap between electronic circuits and fluidics by utilising a channel for solutions to flow through, with electrical interfaces about that channel to perform required analyses. These chips have a very wide range of form-factors, usually dependant on its purpose, and designed to perform one or more specific tasks.

The MFCs used for this project were designed and manufactured as a result of previous work; they were constructed using a transparent, etched layer of photoresist sandwiched between two pieces of silica glass, where each piece of glass had a platinum electrode printed on a titanium trace [24]. As shown in figure 2.2, there were two varieties of this chip, each with a different number of electrode pairs. This was

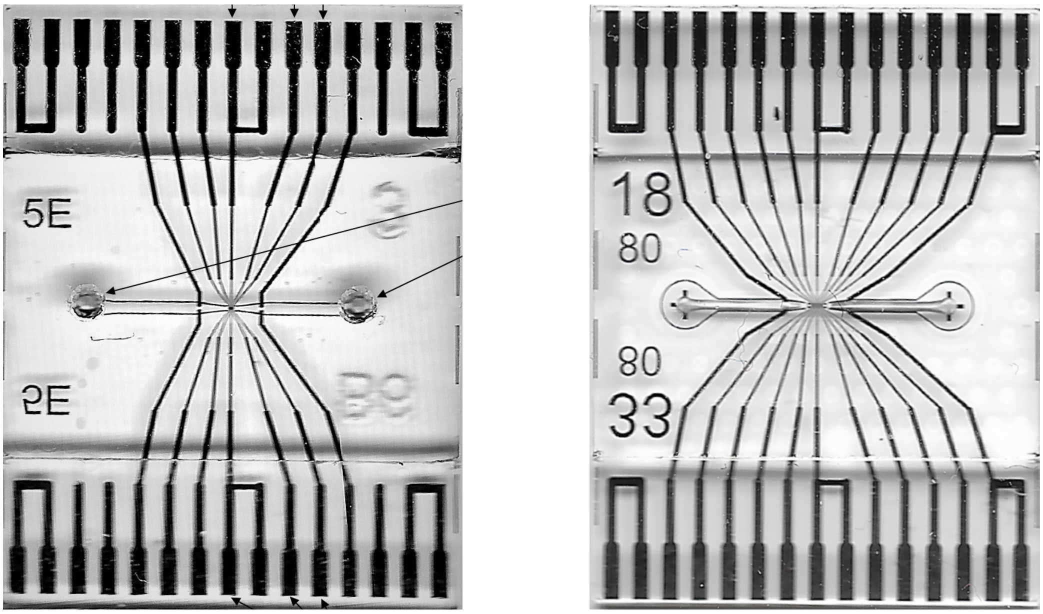

(a) 14 electrode chip

(b) 22 electrode chip

Figure 2.2: MFC designs: Both of these chips were utilised for this project. Figure 2.2a shows the smaller of the two, with 5 inner-electrode pairs, whilst figure 2.2b shows the larger with 9 inner-electode pairs.

useful for varying configurations and performing data collection over a larger length of the channel. Unlike what can be seen in other designs, the two glass sides of these chips were completely independent of one another; electrodes brought into the center of the chip from either side where held parallel from their respective pairings on the other side, forming a capacitor-like look from a 2-D side-on viewpoint. This is shown graphically in figure 2.3.

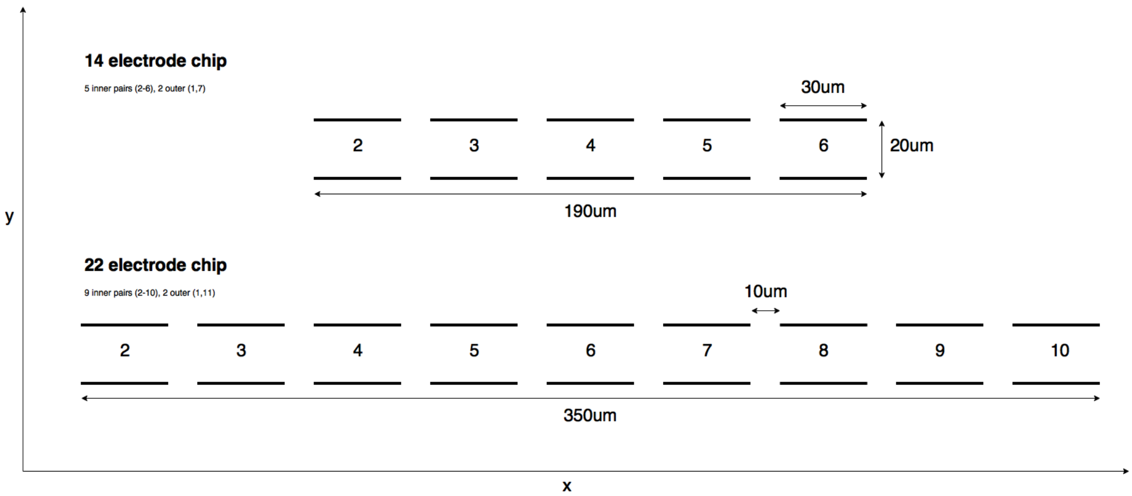

Figure 2.3: MFC cross-sections: A 2-D overview of the cross-section as seen from side-on with the electrodes situated on the top and bottom of the channel.

Chapter 3

Theoretical Analysis

3.1 Channel Modelling

In order to analyse the effects of applying electrical stimuli to the micro-fluidic chips described in section 2.3, an electronic equivalence needed to be generated to allow the appropriate derivations to take place. With this came the need to consider how saline would behave when a potential difference was applied across it.

3.1.1 The Electrical Double Layer

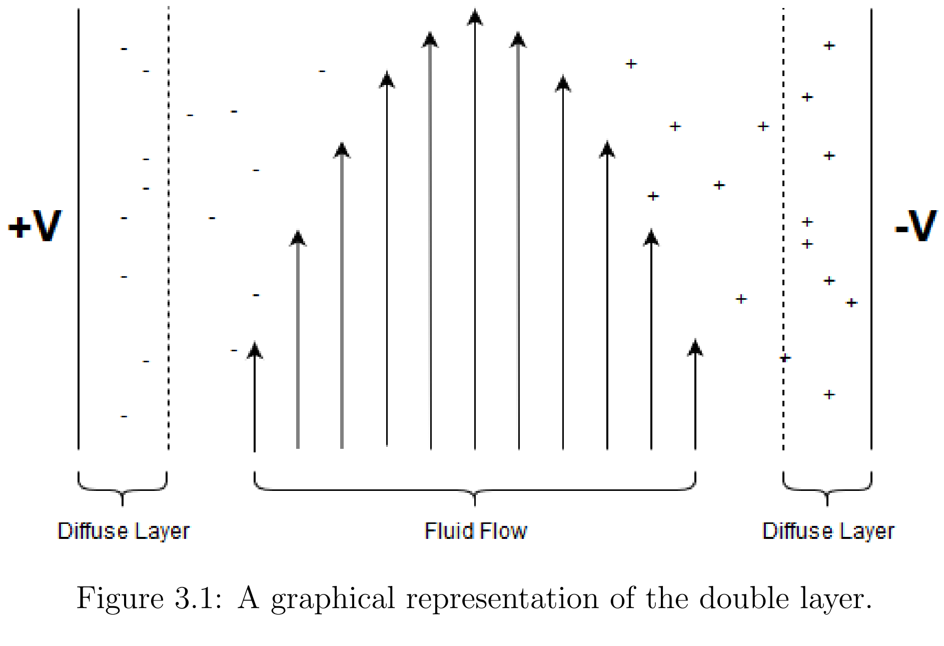

Figure 3.1: A graphical representation of the double layer.

Under the assumption that a DC voltage has been applied between the capacitive plates shown in figure 3.1, an accumulation of positive ions within the liquid solution builds-up against the negatively charged plate, and the opposite occurs against the positively charged plate. This eventuality, coupled with the minute distance between the plates and the ions, causes an additional capacitance associated with each plate at the electrode-solution interface; the double-layer capacitance C_{edl}. Whenever an electric potential is applied to a solution in such a manner, these capacitive properties causes the drop in potential to be non-linear.

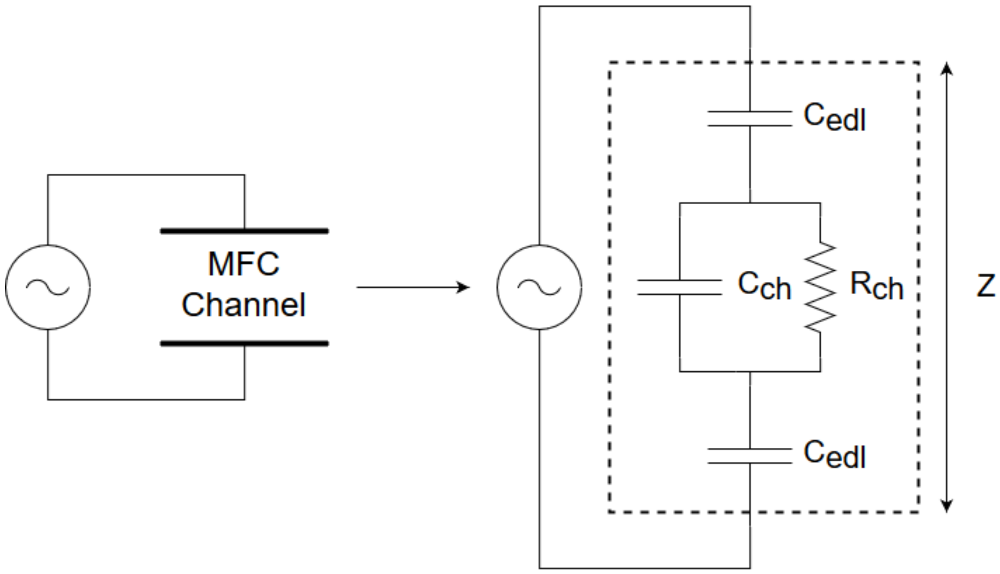

Figure 3.2: Equivalent electrical model of the MFCs electrodes.

As with any capacitance, its impedance effects can be significantly reduced by using an alternating current at high frequencies ($> 10^6$Hz). Considering the EDL capacitance, as well as the resistance and capacitance of the channel itself, an electrical model of the micro-fluidic chip was created. Figure 3.2 shows this model, incorporating both the real and imaginary components of the overall channel impedance Z required to make the model valid for both alternating and direct currents.

3.1.2 Quantifying the Double-layer Capacitance

The EDL capacitance is a series product of two layers of ions; the Stern layer and the diffuse layer. In the simple model of this principle, the diffuse layer is taken as the depth of the entire double-layer by considering all ions as point charges. The Debye length (equation (3.1)) represents the thickness of the diffuse layer. A 1X PBS solution was used for all experimentation, and as a result its properties could be applied to the Debye length equation to solve for the depth of the diffuse layer.

$$\lambda_D = \sqrt{\frac{\epsilon_r \epsilon_0 kT}{2N_A q^2 c_0}} \tag{3.1}$$

$$\lambda_D = \sqrt{\frac{(78.3)(8.85 \times 10^{-12})(1.38 \times 10^{-23})(300)}{2(6.022 \times 10^{23})(1.6 \times 10^{-19})^2(137)}} = 1.32\text{nm} \tag{3.2}$$

Using this derived value for the Debye length, it was possible to calculate a value for C_{edl} using the capacitance equation. The area of the electrode plate is shown in figure 3.3 as being 30μm $\times$ 40μm.

$$C_{edl} = \frac{\epsilon_r \epsilon_0 A}{\lambda_D} \tag{3.3}$$

$$C_{edl} = \frac{(78.3)(8.85 \times 10^{-12})(3 \times 10^{-5})(4 \times 10^{-5})}{1.32 \times 10^{-9}} = 630\text{pF} \tag{3.4}$$

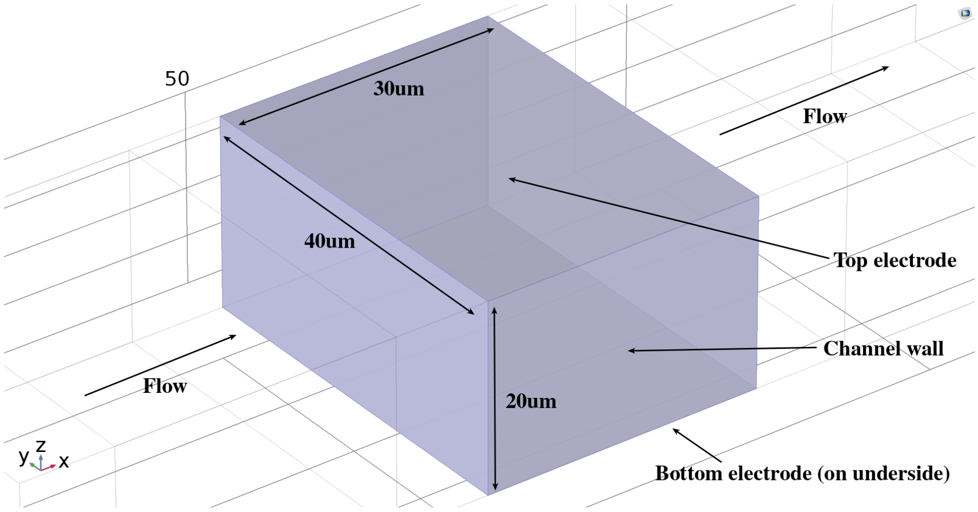

Figure 3.3: A 3-D rendering of a single pair of electrodes highlighting the previously undisclosed dimension of depth.

3.1.3 Electrode Proximity

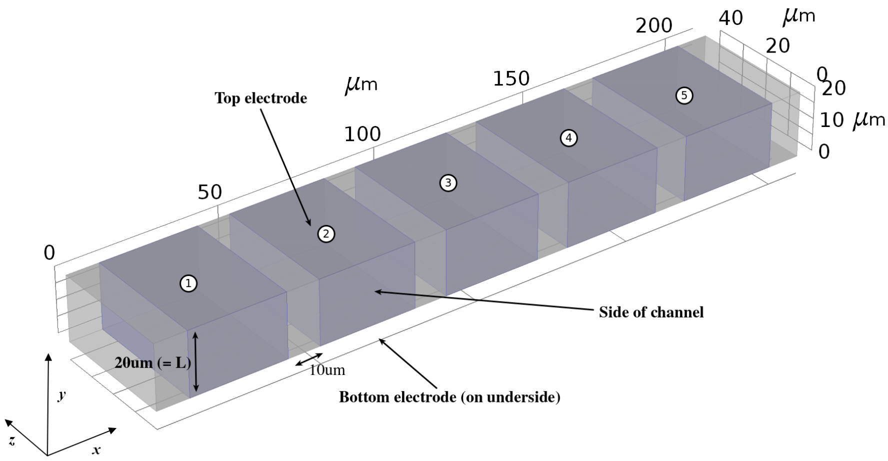

Figure 3.4: A 3-D rendering of the 5 inner-electrode pairs of the chip shown in figure 2.2a.

Unlike a 'standard' parallel plate capacitor, the proximity of the electrode plates along the x-axis causes significant electric field bending towards electrodes in-line with themselves. This is the case because, as shown in figures 2.3 and 3.4, the separation of any two electrodes along the x-axis is only 10μm whilst the separation between parallel electrodes along the y-axis is 20μm. On the application of equation (3.5) for a given Cartesian plane yields two distinct electric field components assuming the z component is negligible.

$$E_c = \frac{U}{L_c} \tag{3.5}$$

$$E_x = \frac{U}{L_x} \tag{3.6}$$

$$E_y = \frac{U}{L_y} = \frac{U}{2L_x} = \frac{1}{2}E_x \tag{3.7}$$

Equations (3.6) and (3.7) show how the electric field intensity along the x-axis is twice as great as that along the y-axis. A *COMSOL Multiphysics*[1] simulation was run for a single electrode being driven at a voltage of $U = 1$V, whilst all other electrodes were connected to ground. The result of this, as shown in figure 3.5, supports the previous calculations and demonstrates how, even with surrounding electrodes being grounded, the electric field diverges through the middle of the medium. This implied that any applied voltage U will drive the center of the channel towards a given fraction of that voltage.

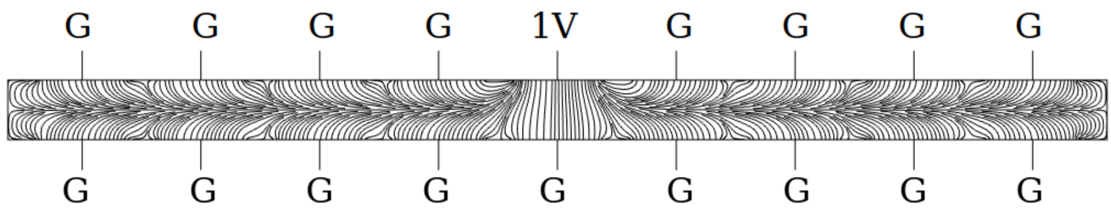

Figure 3.5: Simulation demonstrating dominant electric field bending along the x-axis.

3.1.4 Impedance Analysis

As demonstrated by the electrical equivalent in figure 3.2, the magnitude of the channel impedance $|Z|$ was expressible as a sum of the parallel combination of R_{ch} and X_{ch}, together with the combined reactance of the EDL capacitance X_{edl}. The capacitive effects of C_{ch} are negligeble at or beyond frequencies of around 10^6Hz [24], and thus could be discounted from equation (3.8).

$$|Z| = 2X_{edl} + \left(\frac{1}{R_{\text{ch}}} + \frac{1}{X_{ch}}\right)^{-1} \tag{3.8}$$

$$|Z| \approx 2X_{edl} + R_{ch} \qquad (\text{for } f \geq 10^6\text{Hz}) \tag{3.9}$$

Before a theoretical value for $|Z|$ could be calculated, the channel resistance R_{ch} needed to be approximated. A singular, constant value for R_{ch} was difficult to calculate precisely due to the conductivity of PBS. Normally, a simple calculation for the resistance of a body can be found using equation (3.10), the resistor equation.

$$R_{ch} = \frac{L_y}{\sigma A} \tag{3.10}$$

$$R_{ch} = \frac{2 \times 10^{-5}}{(1.3)(3 \times 10^{-5})(4 \times 10^{-5})} = 12.8\text{k}\Omega \tag{3.11}$$

[1] *COMSOL Multiphysics* v5.3a. `www.comsol.com`

The theory behind the calculation shown in equation (3.11) was flawed however; resistance is a measure of resistivity over a given length, that is to say the length of the resistive body in question. Gaining the result shown required the assumption of a confined area between two parallel electrode plates wherein all of the current across the resultant resistor would have flown. Drawing attention back to figure 3.5, it could be seen that this assumption was false. In fact, current would flow from the driven electrode to all of the surrounding electrodes with varying magnitude. This essentially created a vast network of paths, that could each be seen as a resistor, adding to an overall parallel combination. Therefore, the channel resistance instead needed to be represented by a simple summation incorporating the unknown resistances of *all* these paths. Equation (3.11) instead only represented the resistance *between* the parallel plates R_p, not the channel resistance R_{ch}; a quantity that required experimental investigation to determine, as in chapter 4.

$$\therefore R_p = 12.8\text{k}\Omega \tag{3.12}$$

$$R_{ch} = \left(\sum_{i=1}^{n} \left(\frac{1}{R_i} \right) \right)^{-1} \tag{3.13}$$

Where n is some discrete real number, i is the iteration number and R_i is the resistance for a given path iteration. It was assumed that, with 1X PBS being a good electrical conductor, the value of R_{ch} was to be far smaller than expected by equation (3.11). The implication of the parallel resistor theory, equation (3.13), being that the sum of resistors not in series with one another negate against the total parallel resistance. This lead to the assumption shown by equation (3.15).

$$R_{ch} \ll X_{edl} \qquad (\text{for } f \cong 10^6\text{Hz}) \tag{3.14}$$

$$\therefore |Z| \approx 2X_{edl} \qquad (\text{for } f \cong 10^6\text{Hz}) \tag{3.15}$$

It could also be said, on an adaptation of these assumptions in conjunction with the equivalent circuit (figure 3.2), that eventually a high enough frequency would be reached where the opposite of equations (3.14) and (3.15) could be proven valid:

$$X_{edl} \to 0 \qquad (\text{for } f \gg 10^6\text{Hz}) \tag{3.16}$$

$$\therefore |Z| \approx R_{ch} \qquad (\text{for } f \gg 10^6\text{Hz}) \tag{3.17}$$

3.2 Electrothermal Finite Element Analysis

Before experimentation could begin, the energy dissipation of the heating electrode needed to be considered; an appropriate voltage had to be applied to the channel in order to heat it sufficiently enough to get a response. To calculate such a voltage, a relation was formed between an AC input signal $u(t)$, the impedance of the channel Z and an increase in temperature ΔT for the contained solution of saline. This started with equation (3.18), the equation for power.

$$p(t) = \frac{u(t)^2}{|Z|} \tag{3.18}$$

$$u(t) = U_m \sin(\omega t) \tag{3.19}$$

The average power over a period of time is given by the integral of the sinusoidal input voltage over that period of time. An AC signal can be represented by equation (3.19). By integrating with respect to the time period of the input signal, the average power it provided could be derived.

$$P_{\text{av}} = \frac{U_m^2}{2\pi|Z|}\int_0^{2\pi} \sin^2(\omega t)\ d(\omega t) \tag{3.20}$$

$$= \frac{U_m^2}{4\pi|Z|}\left[\int_0^{2\pi} 1\ d(\omega t) - \int_0^{2\pi} \cos(2\omega t)\ d(\omega t)\right] \tag{3.21}$$

$$= \frac{U_m^2}{2|Z|} \tag{3.22}$$

The rate in which the temperature of a system changes can be defined as the rate of heat added to that system minus the heat taken away. In this case, heat is removed from the system by convection and thus obeys Newton's law of cooling (equation (3.24)), whilst the heat energy added to the system is the average power input as solved in equation (3.22); this is to say that $P_{\text{av}} = \frac{dE}{dt} = \frac{dQ_{\text{in}}}{dt}$.

$$\frac{dT}{dt} = c\left(\frac{dQ_{\text{in}}}{dt} - \frac{dQ_{\text{out}}}{dt}\right) \tag{3.23}$$

$$\frac{dQ_{\text{out}}}{dt} = hA\Delta T \tag{3.24}$$

$$\therefore \frac{dT}{dt} = c\left(\frac{U_m^2}{2|Z_{ch}|} - hA\Delta T\right) \tag{3.25}$$

In order to solve equation (3.25), multiple simulations on *COMSOL Multiphysics* needed to be carried out so that a temperature dissipation pattern could be obtained. The results of these simulations are shown in figure 3.6.

3.3 The Lock-in Amplifier

Lock-in amplifiers are designed to filter out very small AC signals from very noisy environments. Using a technique known as phase-sensitive detection, these devices work using a constant AC reference signal in order to extract a mathematically comparable signal from a given input.

$$u_s(t) = U_s \sin(\omega t) \tag{3.26}$$

$$u_{\text{out}}(t) = HU_s \sin(\omega t + \phi) \tag{3.27}$$

Equation (3.26) shows an arbitrary AC waveform of amplitude U_s. When applied as a supply voltage across a potential divider setup, like shown in figure 3.8, the voltage output from the system can be defined as the supply voltage being attenuated by a factor of H. This is shown by equation (3.27). By taking two of these potential dividers in parallel and connecting both of their outputs to a LIA, a differential voltage reading could be performed.

$$\text{A} = u_x(t) = HU_s \sin(\omega t + \phi_x) \tag{3.28}$$

$$\text{B} = u_y(t) = HU_s \sin(\omega t + \phi_y) \tag{3.29}$$

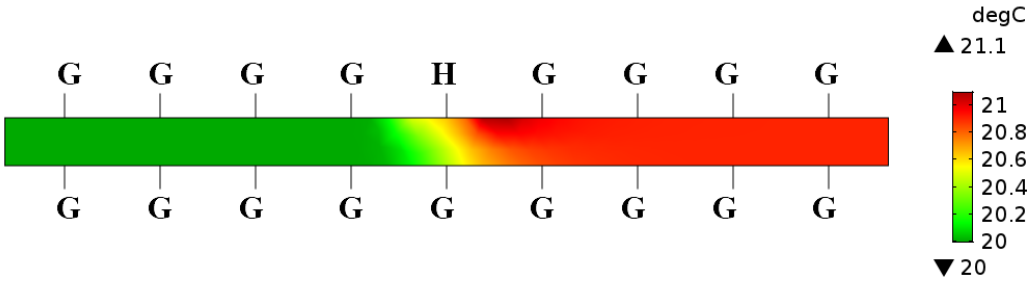

(a) Flow-rate = 5μl/min.

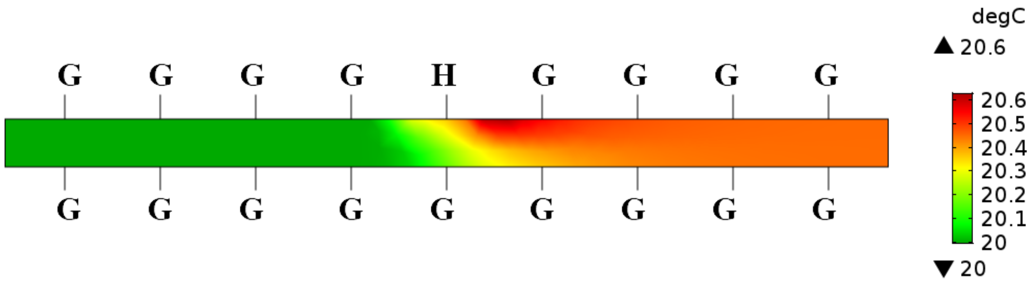

(b) Flow-rate = 10μl/min.

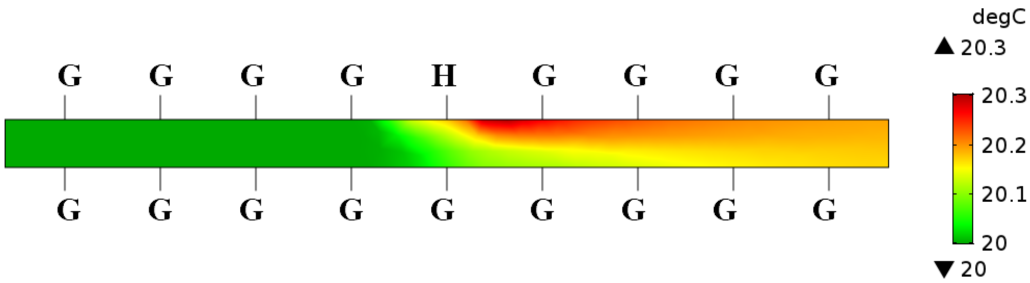

(c) Flow-rate = 25μl/min.

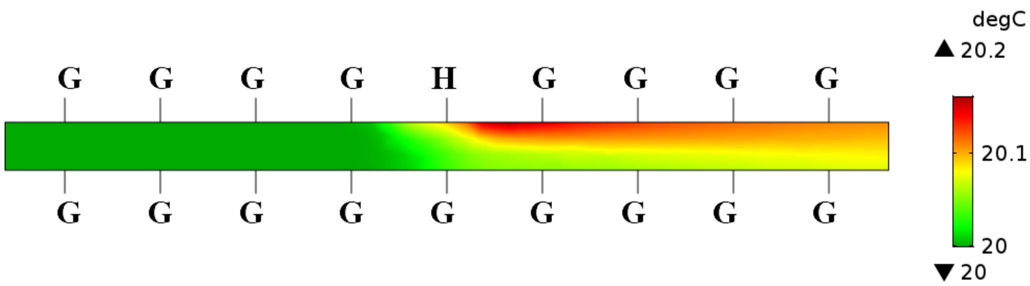

(d) Flow-rate = 50μl/min.

Figure 3.6: Simulated heat dissipation: A set of *COMSOL* simulations identifying how heat was expected to dissipate within the MFC for various flow-rates. The voltage applied to the heating electrode in every case was 10V. These simulations were run in acknowledgement of the non-uniformity of flow-rate within micro-channels as outlined in appendix F, and shown graphically in figure 3.1.

This process yields two distinct input signals, A and B. By inputting these signals, along with the reference voltage $u_s(t)$, a lock-in amplifier is capable of providing the magnitude of the voltage difference ΔU between the two inputs as well as the phase difference $\Delta\phi$ between the differential and reference voltages. An example of this is shown in figure 3.7.

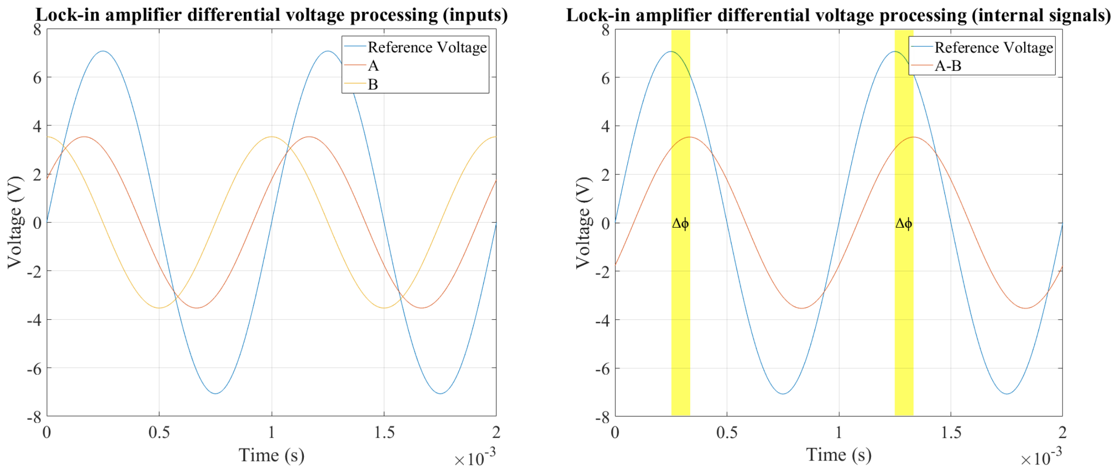

(a) (b)

Figure 3.7: LIA signal overview: The graphs shown here represent how a LIA handles a differential voltage input, then comparing it with some reference voltage.

The lock-in amplifier used for all experimentation was a *Zurich Instruments HF2 series*[2] designed to operate with input frequencies of up to 50MHz. This device was controlled directly by a computer over a USB 2.0 interface; having no controls on the device itself, all operational functions were performed through the device's specialised software, *ziControl*.

3.4 Parallel Potential Dividers and Calorimetry

3.4.1 Summary

In reference to figure 3.8; assuming that all components are ideal, and that the lock-in amplifier's inputs (A and B) were connected to $u_x(t)$ and $u_y(t)$ respectively, equation (3.30) could be shown to be valid. Consequently, the sum $A - B$ will always yield zero regardless of input voltage or frequency.

$$u_x(t) = u_y(t) = u_{\text{ch}}(t) \tag{3.30}$$

However, the concept on which this project was based assumed that a change in fluid properties would elicit a change in the voltage held across the channel. Employing a calorimetric flow-rate sensor topography [1, 21] as described in section 2.2.3, the heating electrode was placed between the two parallel potential divider sensor electrodes enabling fluid velocity to become a detectable factor. Under motion, the fluid could have travelled from X to Y, or vice-versa; the addition of a heat dissipater

[2] *LabOne* edition. `www.zhinst.com/products/hf2li`

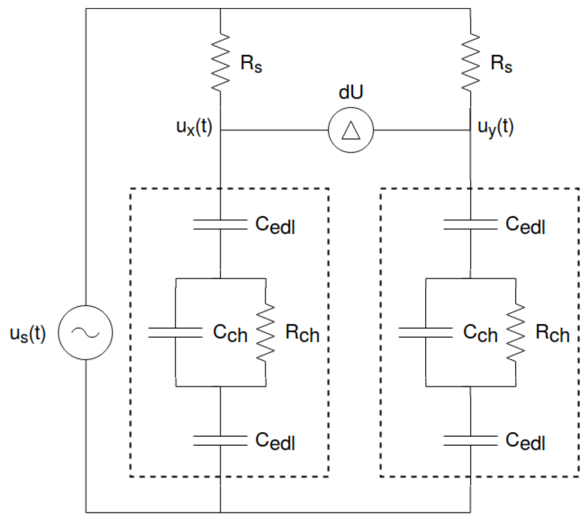

Figure 3.8: The parallel potential divider: This setup consists of two potential divider configurations, as shown in figure 3.2, placed in parallel whilst sharing the same source voltage $u_s(t)$.

between the two enabled heat energy to travel towards either X or Y, dependant on the direction of the fluid's flow.

$$H = \frac{|Z|}{|Z| + R_s} \tag{3.31}$$

The attenuation factor H in equations (3.28) and (3.29) could be represented by equation (3.31), the potential divider equation. As described in section 3.2, since Z was frequency dependant, it also meant that H was frequency dependant. On substitution of equation (3.9) into equation (3.31), an expansion inclusive of the all the required channel properties were found that held valid for the circuit shown in figure 3.8.

$$H = \frac{(2X_{edl} + R_{ch})}{(2X_{edl} + R_{ch}) + R_s} \tag{3.32}$$

Working with the assumption that H is, in some way, dependant on temperature T, it became possible to analyse how a temperature difference between sections of the channel would have caused the voltage held across those respective sections to differ from one another. Taking the difference between these voltages would have therefore resulted in $\Delta U \neq 0$. Since temperature, as shown in figure 3.6, is dependant on flow-rate, it was also valid to say that ΔU was dependant on flow-rate as well.

3.4.2 PBS and its Temperature Dependency

The conductivity σ of a particular medium can be shown to be dependant on its temperature. As with almost all fluids, an increase in temperature relates to a decrease in its viscosity [25], which in turn translates into an increase in conductivity. As a liquid substance becomes less viscous, it is capable of moving with less resistance - it flows far more easily. These effects also apply within the liquid itself where ionic movement also requires less work to carry out, leading to a larger electrical current on the application of a potential difference [26]. In the case of a solution of PBS, its conductivity is also defined by the concentration of the solution. For reference, 1X PBS has a recipe defined by the quantities shown in table 3.1.

Ingredient	**Molecular Weight (g/mol)**	**Molarity**
Soduim Chloride (NaCl)	58.4	137mM
Potassium Chloride (KCl)	74.6	2.7mM
Disodium Phosphate (Na_2HPO_4)	142	10mM
Potassium Phosphate (KH_2PO_4)	136	1.8mM

Table 3.1: The recipe for a 1X solution of PBS[3].

Since it was already known that σ would change with T, it was important to gain an idea of how this would effect the value of R_{ch}. Though this value, for reasons stated in section 3.1.4, had not yet been determined, the theoretical resistance between two parallel plates R_p (equation (3.13)) was used in its place. This was merely as a reference to gauge how any change in conductivity would have effected the system before experimentation took place.

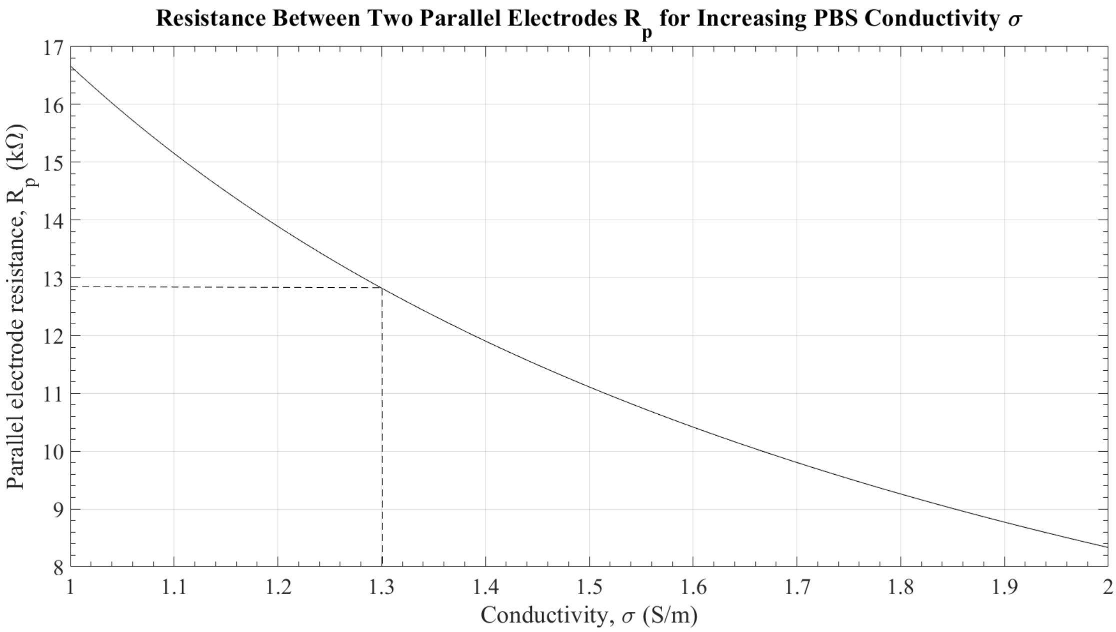

Figure 3.9: PBS conductivity variation.

Though the actual change in conductivity was not known with respect to temperature, this was possible to explore once sufficient experimental data had been collected. The dashed line in figure 3.9 represents the approximate documented value of σ for the PBS solution used here, yielding a value comparable to that of the parallel electrode resistance R_p (equation (3.12)).

[3]As defined by *AAT Bioquest* to prepare 1L of 1X PBS. `www.aatbio.com/resources/buffer-preparations-and-recipes/pbs-phosphate-buffered-saline`

Chapter 4

RC Response Analysis

4.1 Experimental Methodology

The first experiment run for this project came in the form of a basic RC response analysis. As described in chapter 3, the impedance of the channel was a function of frequency, and thus changed based on this input parameter. Input frequency was cycled between 1MHz, the minimum required frequency to overcome the channel capacitance C_{ch}, and 50MHz, the upper frequency limit of the measurement hardware.

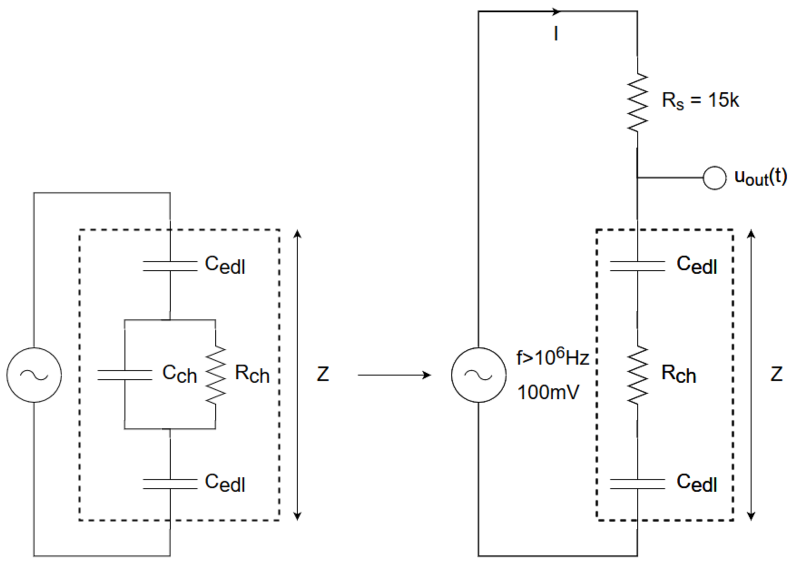

Figure 4.1: Experimental setup for the RC response analysis.

The experimental setup used here is shown in figure 4.1. This circuit consisted of a single potential divider; a 15kΩ resistor on top with a channel electrode underneath, forming an RC network. All other electrodes were connected to ground, creating an electric divergence field much like that seen in figure 3.5. The input voltage $u_s(t)$ was set to an amplitude of $U_s = 0.1$V for all measurements in this investigation.

$$|Z| \approx 2X_{edl} \qquad (\text{for } f \cong 10^6\text{Hz}) \qquad (3.15)$$

$$|Z| \approx R_{ch} \qquad (\text{for } f \gg 10^6\text{Hz}) \qquad (3.17)$$

Using the assumptions and theory outlined in section 3.1.4, a simulation was carried-out in order to identify the trend that was to be expected through experimentation. Equation (3.17) demonstrates how, at frequencies in the order of 10^7Hz, the channel impedance $|Z|$ minimises to just R_{ch}. Since the value of this quantity was not known, the theoretical approximation used only equation (3.15); this meant that it was likely there would have been a discrepancy between the expected and observed responses at high frequencies.

Before experimentation begun, the MFC was flushed through with deionised water and subsequently with a 1X solution of PBS to ensure all potential contaminants had been expelled. Data was collected rapidly using the built-in sweeping utility of the *HF2 LI*, configured to a logarithmic sweep consisting of 100 points-per-decade and 4-times averaging.

4.2 Results and Analysis

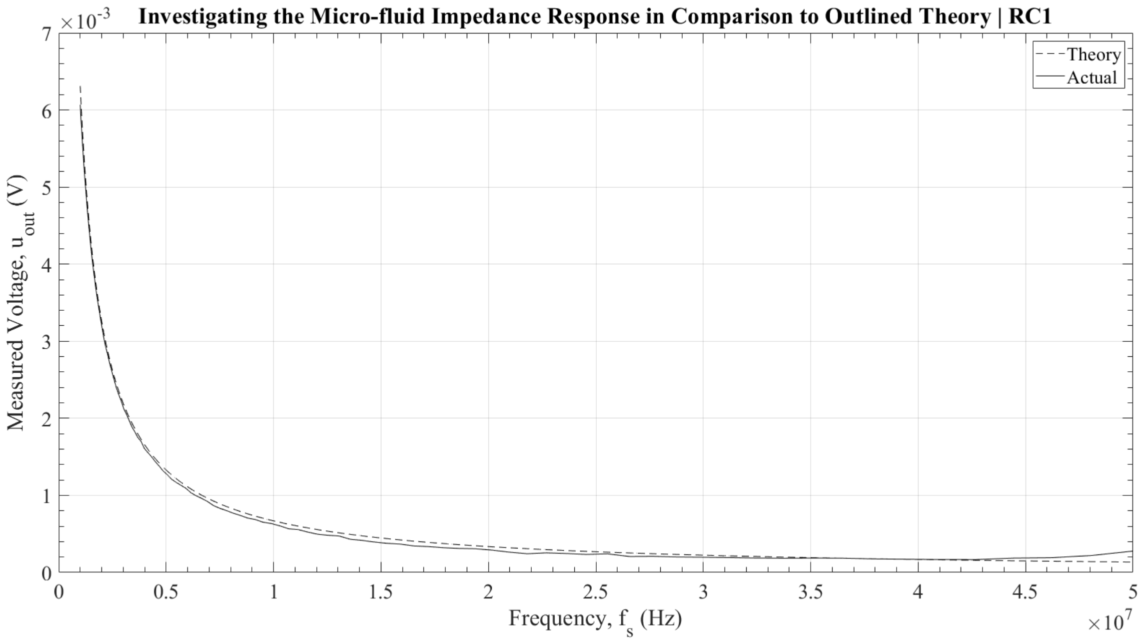

Figure 4.2: A comparison between theoretical and measured frequency responses.

As seen in figure 4.2, the actual trend is almost identical to that of the theory. It was also noticed that the measured voltage did in-fact level out beyond approximately 35MHz. The voltage reading also began to rise towards the 50MHz frequency point, notably due to the operating limitations of the LIA. Since the response was as expected, it was possible to work backwards and identify, accurately, the actual value of R_{ch}.

As theorised previously, the total channel impedance $|Z|$ was dominated by the double-layer reactance X_{edl} for $1 \times 10^6 \leq f_s \lesssim 2.9 \times 10^7$Hz. Within the range $2.9 \times 10^7 \lesssim f_s \lesssim 4.6 \times 10^7$Hz, the channel impedance holds relatively steady; the implication of this being that, as stated by equation (3.17), the channel resistance R_{ch} was dominant here. Figure 4.3a shows, through numerical manipulation, exactly

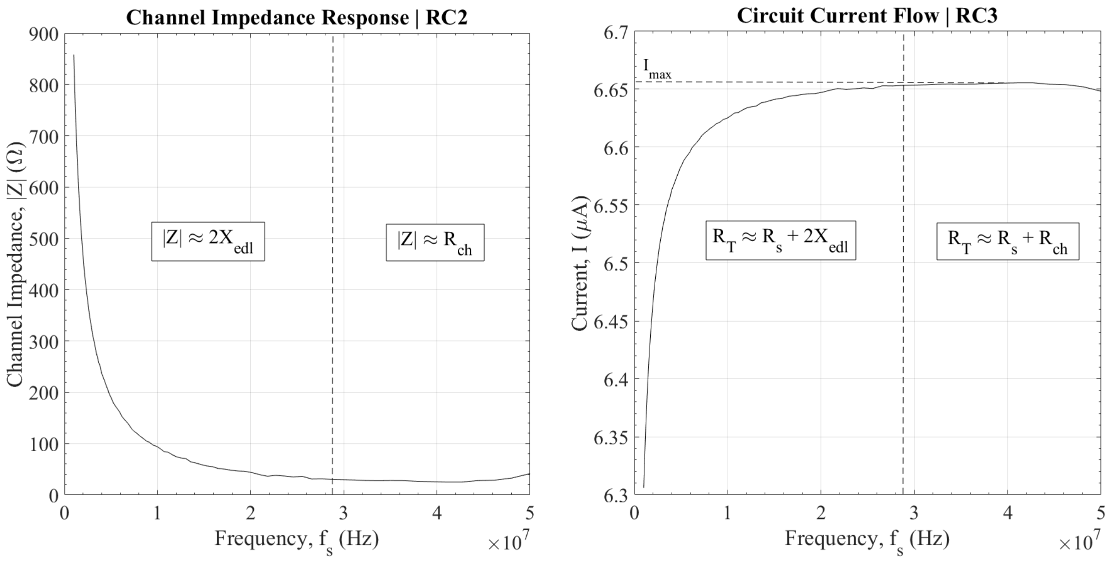

(a) (b)

Figure 4.3: Channel impedance and circuit current as a function of frequency.

what value $|Z|$ held for a given frequency input. By looking at the higher frequencies on this graph, an estimation for R_{ch} could be found:

$$R_{ch} = 28.5\Omega \pm 2\Omega \tag{4.1}$$

Whilst this may have been sufficient, a more accurate result was obtained through the use of Ohm's law and was used as a method of verifying this numerical approximation, which was read directly from figure 4.3a. The current through both R_s and Z, at any frequency, must have been the same. From this it was possible to identify the peak current $I_{\max}$ through the entire circuit. This point is coupled with that at which the channel voltage, as shown in figure 4.2, was at its minimum value $U_{\min}$.

$$\begin{aligned} R_{ch} &= \frac{U_{\min}}{I_{\max}} && (4.2) \\ &= \frac{(2 \times 10^{-4})}{(6.66 \times 10^{-6})} && (4.3) \\ &= 30\Omega && (4.4) \end{aligned}$$

The value shown in equation (4.4) was in-line with what was expected, as well as in-line with the bounds represented by equation (4.1).

Chapter 5

Methods and Materials

5.1 General Experimental Methodology

Three different calorimetric flow-rate sensor designs were used during experimentation for this project, where each were tested in accordance to the procedures outlined here. Any extra investigations carried out for a given design is stated in the section appropriate to that design. As stated previously the lock-in amplifier used here was a *Zurich Instruments HF2 series*. The device was configured in differential input mode, thereby taking the difference between inputs A and B. As shown by equations (3.28) and (3.29), the voltages being input into these ports were $u_x(t)$ (upstream) and $u_y(t)$ (downstream) respectively. As a result of previous research, an optimal heater operating frequency was found to be 1MHz [27]; a value also sufficiently high enough to ensure that neglecting the channel capacitance C_{ch} remained appropriate. Using the simulations shown in figure 3.6, a peak heater voltage of $U_m = 10$V was selected as being the most appropriate for effective and detectable heat generation.

$$u_h(t) = 10\sin(2\pi \times 10^6 t) \tag{5.1}$$

With regard to the sensors, their voltages U_s were selected to be 100mV. This value was in line with that used previously for the experiment conducted in chapter 4, whilst ensuring the sensors generated very little heat themselves. The sensor frequency was also set to 1MHz by default.

$$u_s(t) = 0.1\sin(2\pi \times 10^6 t) = \frac{1}{100}u_h(t) \tag{5.2}$$

In the case of the fluidic-side of the experiment, saline was input and had it's flow-rate regulated by a *CHEMYX Fusion 400* micro-flow syringe pump[1] capable of accurately creating flow-rates as low as 2pL/min. A *BD Plastic* syringe with a 1mL capacity was used for the longer running, higher flow-rate samples whilst a 500μL glass *Hamilton* was used to hold lower flow-rate samples more steady when required. The chips used were each cleaned and flushed-through using deionised water after each experiment, and saline was run through them before each experiment begun. This ensured any

[1] Now discontinued (2017). `www.chemyx.com/products/fusion-400/`

air bubbles left-over from changing the syringe were purged from the system, as well as any deionised water left-over from the cleaning process.

A 1X solution of PBS was made using a single tablet designed to be dissolved in 200mL of deionised water. Upon dissolving, the solution had a pH of 7.4, and had a recipe in-line with that shown in table 3.1. The PBS tablets themselves, as well as the glass jar used to hold the solution, offered easy access to potential contaminants such as dust, which could have easily gone unnoticed on their surfaces at the time of mixing. Not only did these contaminants risk affecting the measurement data, they also risked blocking the channel, to which the MFC would have needed to be replaced. In order to reduce these risks, the PBS was filtered multiple times before use and transferred out of the glass jar using single-use, disposable and sterile *BD Plastic* syringes. The use of a glass *Hamilton* for transferring the PBS was avoided since these syringes were used repeatedly, and were subsequently far more likely to introduce contaminants into the system.

The flow-rates of interest for POCT applications[2] were between 5 and 50μl/min, and therefore experiments were adjusted to measure at intervals between these values. Three time-lapse data samples were taken for each system configuration using fresh saline-filled syringes. Over an entire sample length each flow-rate was maintained by the syringe pump for a period of one minute to ensure the system had time to stabilise, and an accurate sensor reading could be recorded. This also enabled any drift in measurements to be observed, showing when the settling time was too long or the system unstable. For every dataset recorded, flow-rate was always incremented from low to high, starting at 5μl/min and finishing at 50μl/min, in logarithmic steps.

The circuits powering the sensor designs, outlined ahead in section 5.2, were constructed on prefabricated breakout-boards made specifically to work with the MFCs shown in figure 2.2. Each PCB had 4 input/output connection pads, onto which BNC terminals were soldered where appropriate. On top of this, these boards also had a built-in ground plane that was tied-in to the LIAs ground source (earth) through BNC signal cables that carry a common ground signal in their outer sheath. Due to the nature of how these boards were connected to the MFC, two were populated with the appropriate components for a given configuration; one controlling the electrodes on the top of the channel, the other controlling those on the bottom. These breakout boards were designed to operate both the smaller and larger MFCs (figure 2.2).

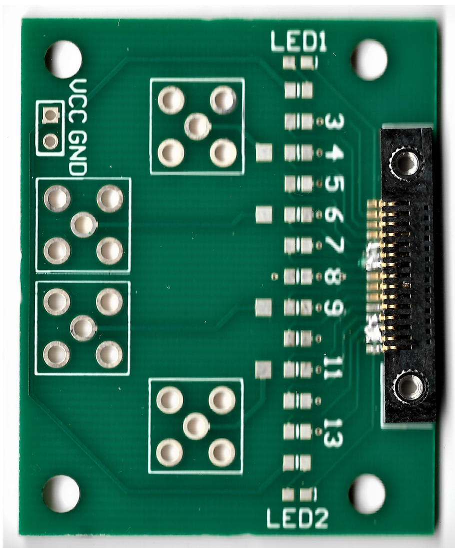

Figure 5.1: A prefabricated, unpopulated breakout PCB.

[2]For many experiments conducted within the *Center for Hybrid Biodevices* at the *University of Southampton*

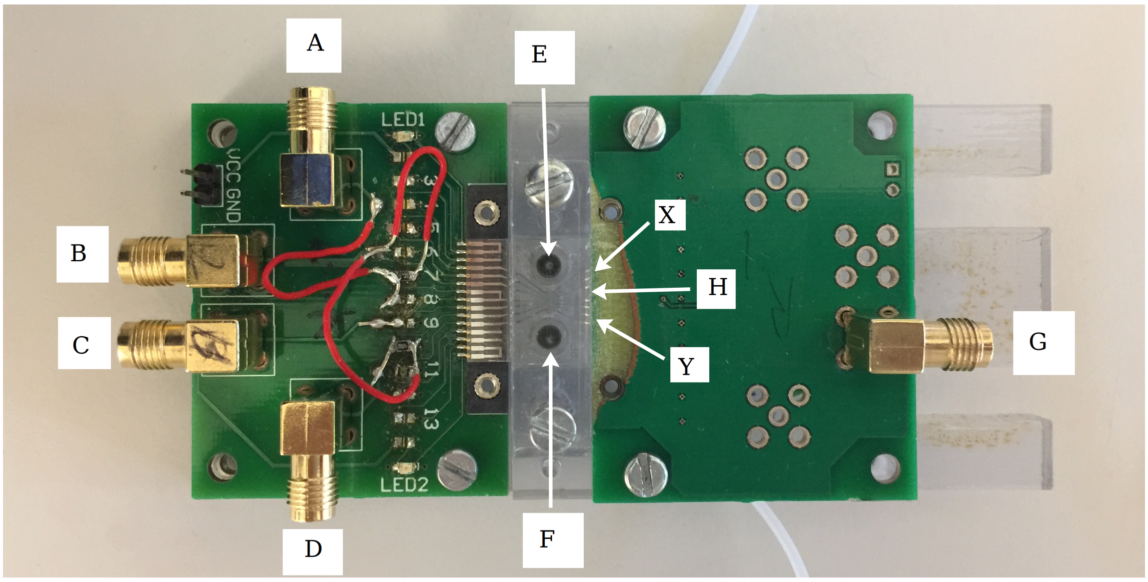

Figure 5.2: MFC casing: The hardware designed to hold the MFC securely in place throughout experimentation. **A:** $u_x(t)$ output terminal. **B:** $u_s(t)$ input terminal. **C:** $u_h(t)$ input terminal. **D:** $u_y(t)$ output terminal. **E:** Fluid inlet. **F:** Fluid outlet. **G:** Ground connection terminal. ***X:*** Upstream sensor electrode. ***H:*** Heater electrode(s)[3]. ***Y:*** Downstream sensor electrode. *Labels in italic represent the physical order of the electrodes as configured within the MFC itself.*

The MFC and surrounding circuitry was held in place by a pre-designed casing board [24] as seen in figure 5.2. This figure shows the implementation of the circuit design shown in figure 5.4, though the physical setup remained identical for all designs with only minor changes to the terminal and on-board connections. No modifications were applied directly to the any of the MFCs, and subsequently they could be 'hot-swapped' when required. The plastic inlet and outlet tubing, which can be seen in figure 5.2, was secured in-place during experimentation as any sudden movements, compression or expansion of these components would have caused disruptive effect on the flow-rate at the micro-scale inside the chips.

5.2 Flow-rate Sensor Designs

5.2.1 Overview

In order to gauge the effects of varying the physical layout of the heaters and sensors within the micro-fluidic channel, three designs were drawn-up to ensure that a sufficient range of different physical conditions could be tested. These designs focussed primarily on varying the magnitude of the heat energy input through the application of multiple heaters, as well as the modification of the sensors to work more effectively. There were, however, certain elements that needed to remain the same between all of the designs.

Firstly, all unused electrodes were connected to ground to minimise electrical interference from external sources. Furthermore, sensors were always separated, by

[3]When multiple heater electrodes were used, all remained in-between X and Y.

at least one grounded electrode, from any heaters. Since $u_h(t) \gg u_s(t)$, placing a heater and sensor side-by-side would have caused severe 'crosstalk' between the two, subsequently resulting in unreliable sensor data. Also, the sensor circuitry itself was maintained for all of the explored designs, only the power rail configurations were changed here. The sensor resistor R_s held a constant value of 15kΩ throughout and was based on the resistance held between any two parallel electrodes, R_p (equation (3.12)). Though not indicative of the overall channel impedance $|Z|$, the experiment carried out in chapter 4 had not yet been conducted, and subsequently the closest resistor value available to that of R_p was selected and placed in the circuit as R_s. The original calculation for this property can be seen on page 11.

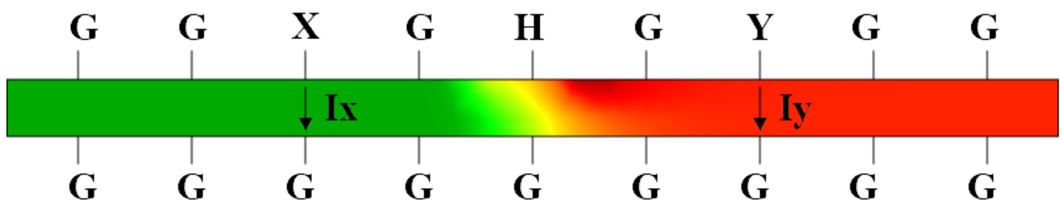

Figure 5.3: Micro-thermal flow-rate sensor example: In this case, where X and Y are sensor voltages, the cooler temperature at X will create a lower current Ix between it and ground, therefore the voltage here will be higher than at Y, where the higher temperature will cause the opposite.

In continuation of the similarities carried between the designs; unlike that utilised for the experiment outlined in chapter 4, two sensor electrodes were setup within the channel, and therefore two of the aforementioned potential divider setups were required to run them. In these experiments, the difference in measured voltage was taken between these two sensors. Theory outlined in section 3.4.2 demonstrates how, upon being either heated or cooled, a liquid solution's conductivity will change.

Applied to all of these designs, an individual sensor's voltage will drop on increasing temperature, and vice-versa. For a given flow-rate in one direction, the temperature for one of these two sensors would be higher than the other, therefore a voltage difference would have been formed between the two and a flow-rate became detectable. Situated between these sensor electrodes were one or more heaters. Heaters were driven directly by an external power supply and contained no in-line components; as much energy as possible was dissipated directly into the channel. This formed the most basic rendition of a calorimetric flow-rate sensor.

5.2.2 Single Heater

An initial design, based solely on the theory outlined in chapter 3, was created consisting of a single heater surrounded by the two sensors, with single-ground spacing. It was both designed and tested to prove the ideas behind this project and built to be expanded on. This design was used in conjunction with the smaller MFC (figure 2.2a).

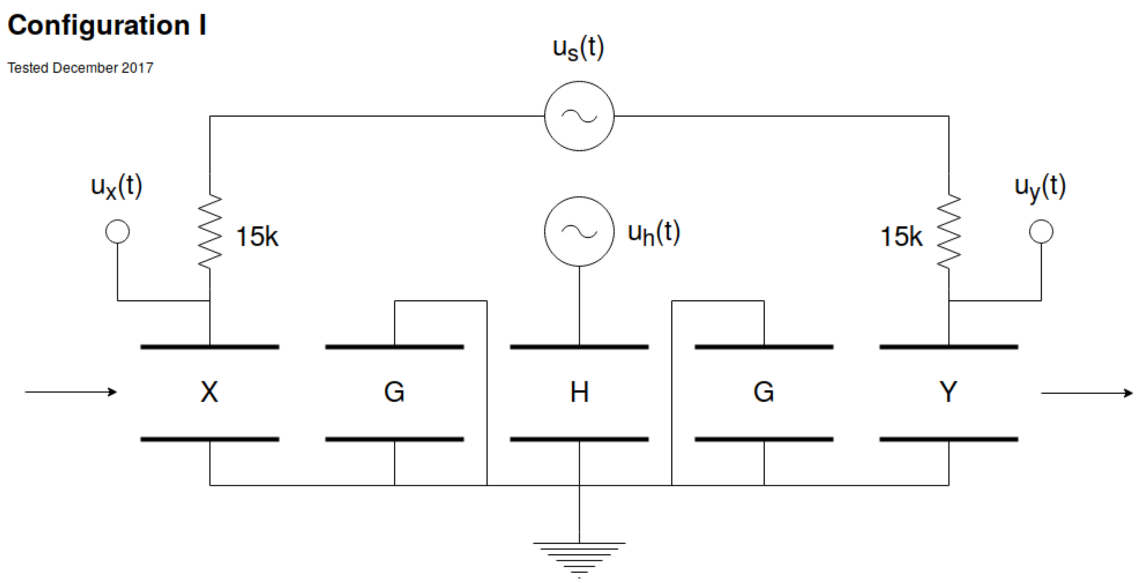

Figure 5.4: Configuration I: Single-spaced, dual sensor setup with a single centred heating element.

5.2.3 Multiple Heaters

The second design began exploring how the application of multiple heaters to the system would either benefit or damage its overall performance. Two additional heaters were added to extend the footprint of the previous configuration shown in figure 5.4. In this case, a total of three heaters were driven by $u_h(t)$ and placed centre-channel. Due to the extended nature of this configuration, the larger MFC shown in figure 2.2b was utilised in place of the smaller one used previously.

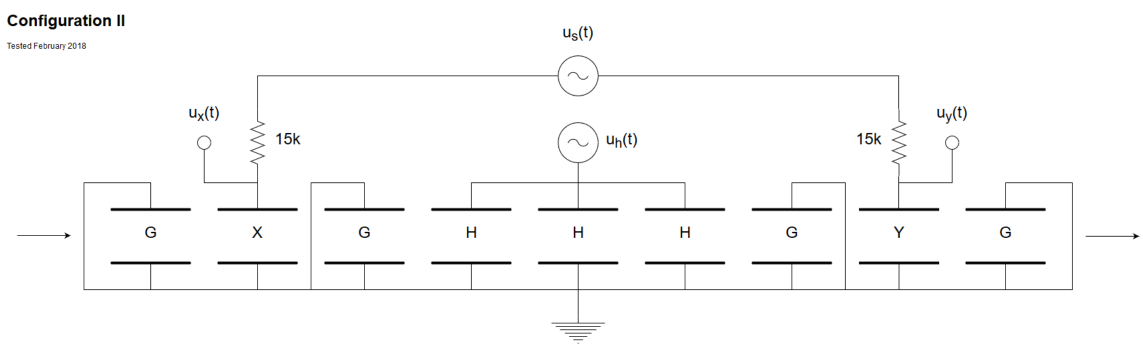

Figure 5.5: Configuration II: Single-spaced, dual sensor setup with three centred heating elements.

To ensure that the addition of more heaters to the channel would not cause any undesirable side-effects, further *COMSOL Multiphysics* simulations were run to anticipate the heat dissipation patterns, and resultant peak temperatures, ensuring that they were not excessive and still fit-for-purpose. A comparative summary of the previous simulations as seen on page 14, against the updated simulations as shown in appendix G, can be seen in table 5.1.

Flow-rate (μl/min)	**Peak Temperature ($^\circ$C)**

	One Heater	***Three Heaters***
5	21.1	22.4
10	20.6	21.2
25	20.3	20.5
50	20.2	20.3

Table 5.1: Summarising theoretical peak downstream channel temperatures.

5.2.4 Single Heater with Floating Sensors

The third and final design was, in contrast, a reduction on the first. Once again returning to the use of a single heater, this design utilised passive sensors without an input voltage of their own; this was to say that $u_s(t) = 0$.

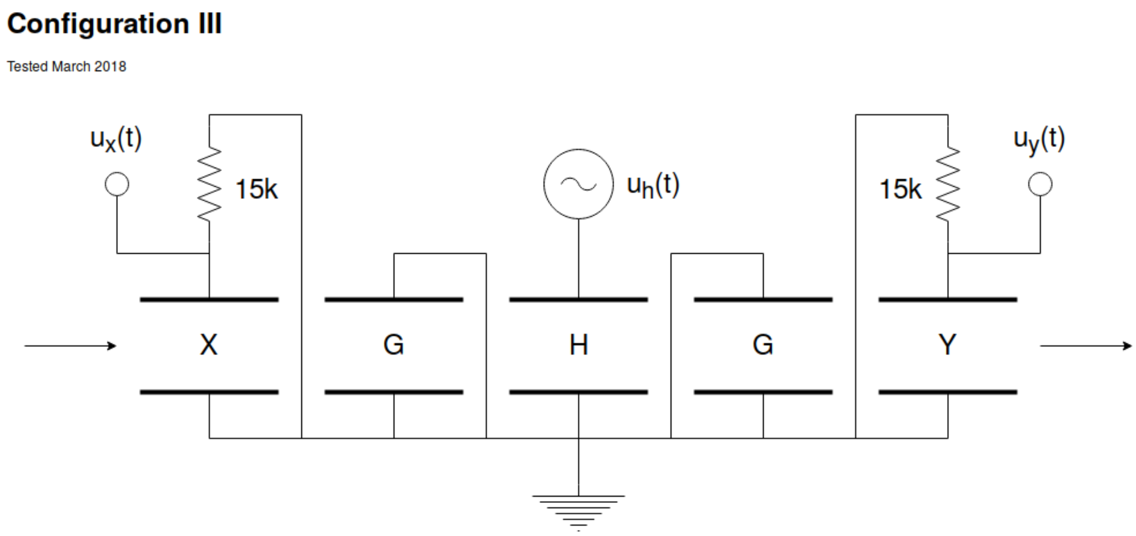

Figure 5.6: Configuration III: Single-spaced, dual floating sensor setup with a single centred heating element.

This passive sensor design consisted of the same potential divider implemented for the sensors in the other designs, but was instead grounded on both sides. Under these conditions the voltage between the ground connections, that is to say at the sensor electrode, was driven by the heater's electric field propagating along the channel itself. This concept was discussed in section 3.1.3, where the electric field of any electrode driven at some given voltage was stronger between those on the same side of the channel, as opposed to those across from it. Also, as detailed in section 3.4.2, the conductivity of any fluid substance is dependant on temperature. In this configuration, the idea was to allow the *heater's* electric field to be effected by this temperature change, in contrast to the sensor's. The effect on the electric field would then subsequently effect the voltage the sensor electrodes were floating at.

The sensor electrodes could be seen to be partially driven through the heating electrodes by analysing the electric field interference patterns. Figure 5.7a acts as a representative example of how both the driven sensors, with an AC applied voltage $u_s(t)$, and any driven heaters, with an AC applied voltage $u_h(t)$, electrically interfere

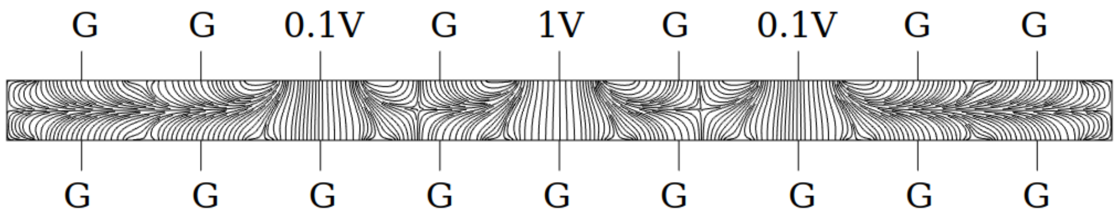

(a) Electric field divergence for configuration I.

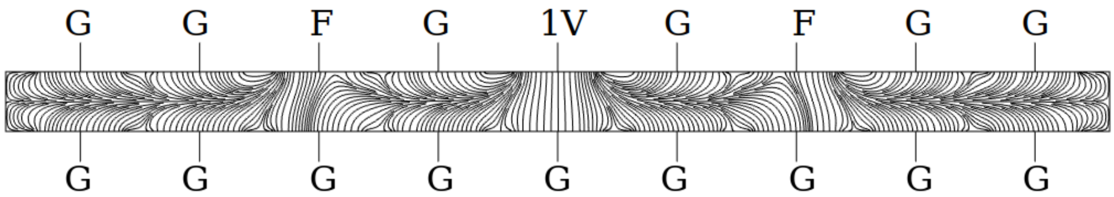

(b) Electric field divergence for configuration III.

Figure 5.7: The theory behind configuration III.

down the length of the channel. Since the sensor electrodes were passive in this configuration; any possible interference between input signals was negated since there was only one, $u_h(t)$. As shown by the simulation in figure 5.7b, the electric field lines from the heating electrode are incident on the sensor electrodes, bringing them both up towards some voltage greater than zero.

Chapter 6

Calorimetric Implementations: Results and Analysis

6.1 Overview and Experimental Outputs

As explained by the general methodology in section 5.1, each configuration generated three time-lapse plots, from which voltage levels specific to certain flow-rates could be determined, as well as how these levels changed between both higher and lower flow-rates. The raw time-lapse data for the single heater, multiple heaters and floating sensors are shown on pages 29, 30 and 31 respectively. Following is a thorough analysis of what these graphs show, as well as what can be inferred from them. In order to collate all of the information gathered as a result of the exhaustive experimentation carried out for this project, table 6.1 was populated with a brief summary of the strengths and weaknesses for each of these three system designs.

#	Strengths	Weaknesses
I	Concept proven with detectable voltage changes between flow-rates and observable levels for ΔU relating to specific flow-rates.	Significant drift with instability at low flow-rates.
II	No identifiable strengths, particularly in comparison to the other two designs.	Insignificant response at any flow-rate, with almost indistinguishable levels for ΔU. Heavy drift as a result of additional channel heaters.
III	Far greater sensitivity to different flow-rates with values for ΔU ranging across the mV rather than the μV range.	Voltage levels for ΔU still drift slightly, though these drifts are more predictable than those seen in other configurations and make up a smaller overall proportion of the signal in comparison to the initial design.

Table 6.1: An overview of configurations and their effects on flow-rate measurements.

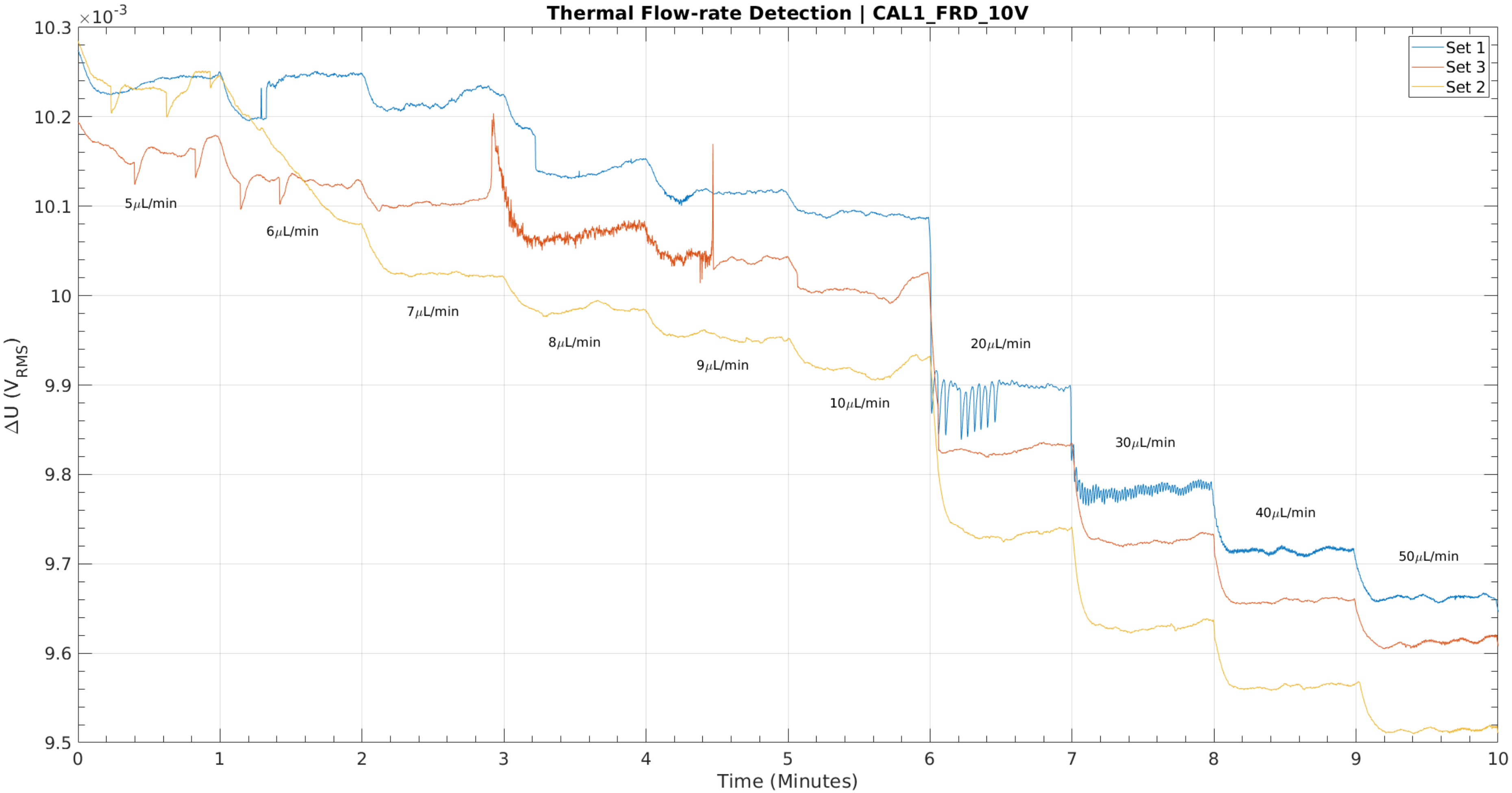

Figure 6.1: Time-lapse variance in ΔU for scaled increases in flow-rate c_v when using the configuration shown in figure 5.4.

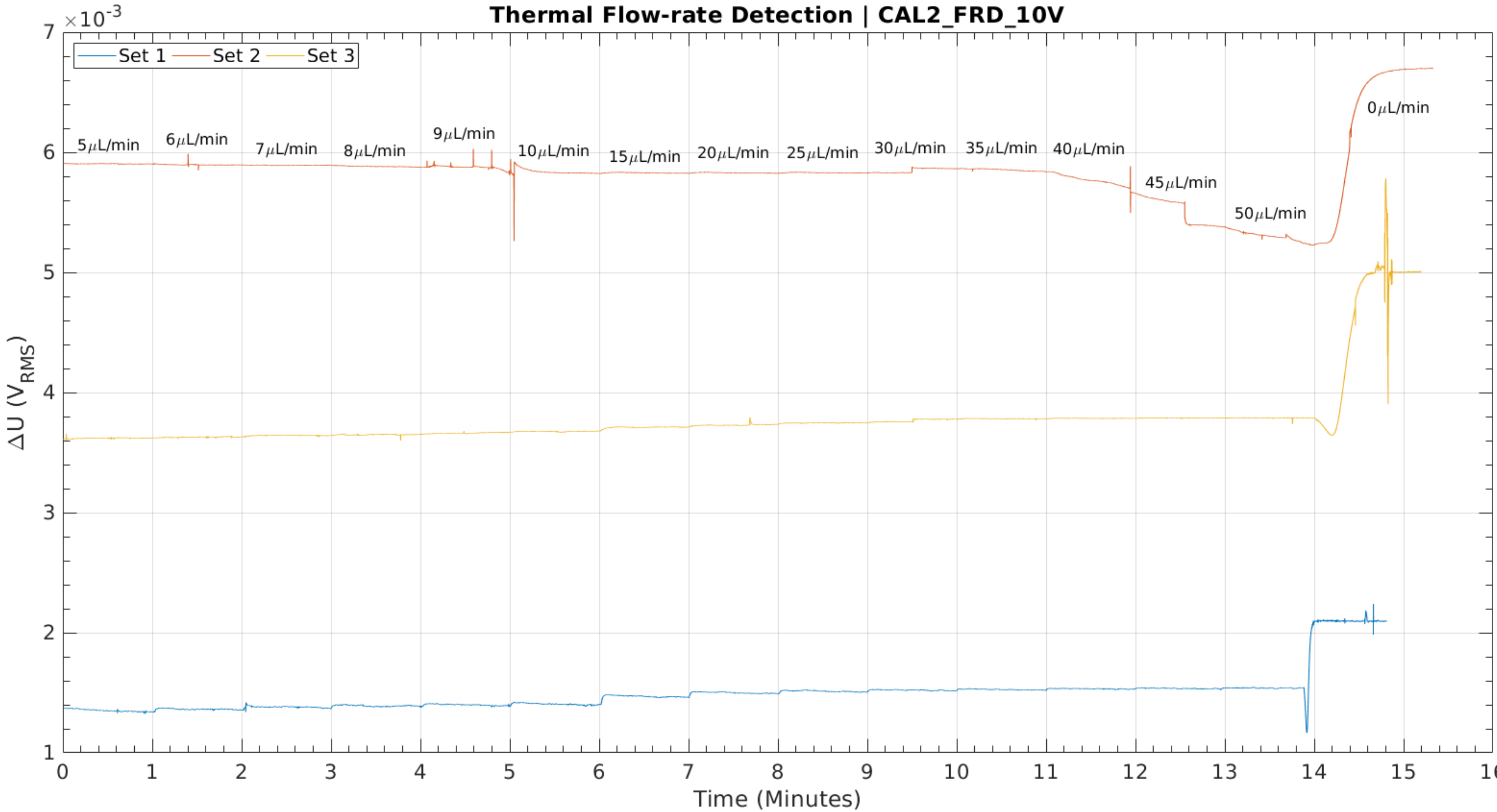

Figure 6.2: Time-lapse variance in ΔU for scaled increases in flow-rate c_v when using the configuration shown in figure 5.5.

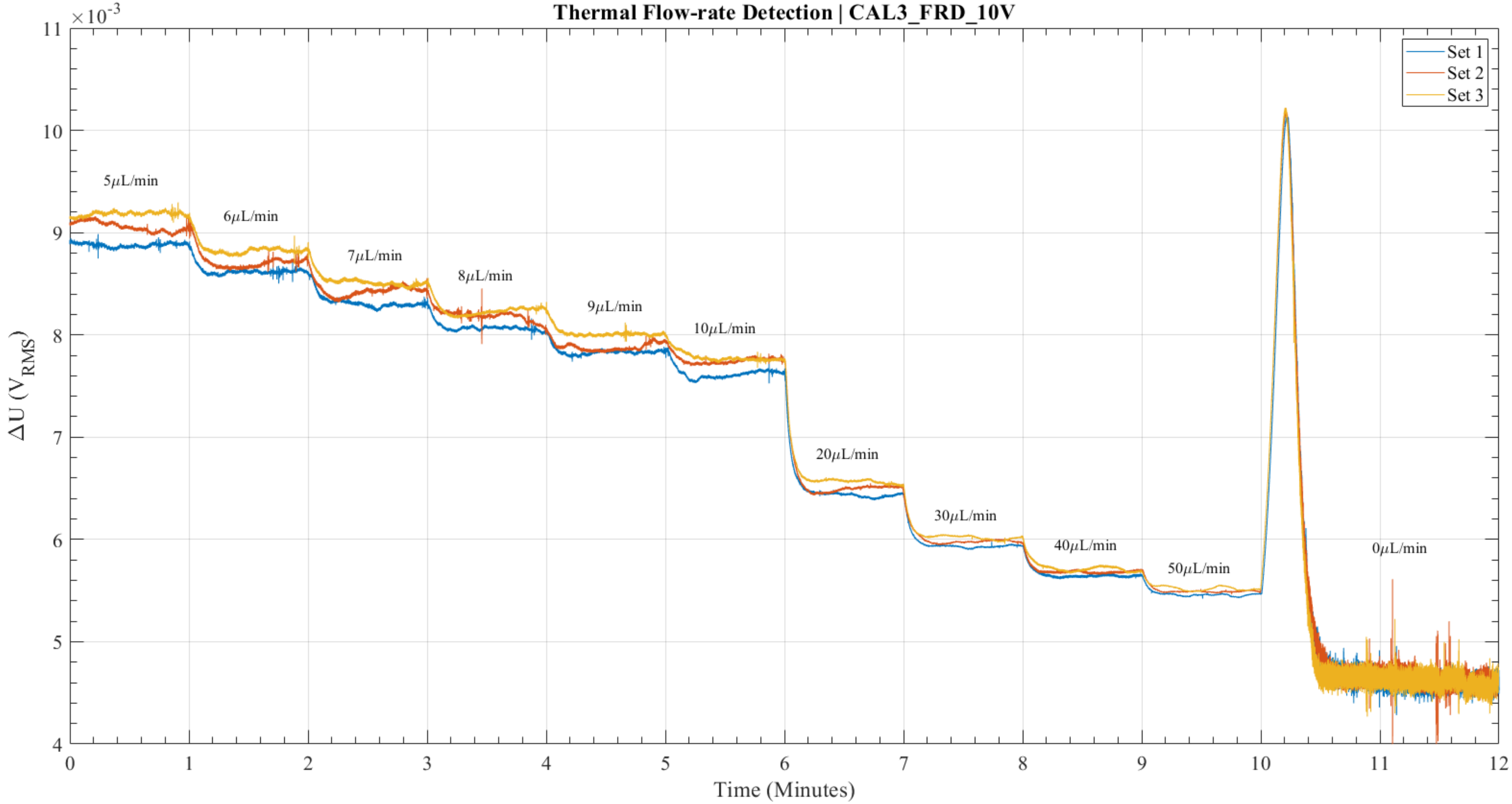

Figure 6.3: Time-lapse variance in ΔU for scaled increases in flow-rate c_v when using the configuration shown in figure 5.6.

6.2 Single Heater

After testing the initial configuration extensively, the concept behind flow-rate detection of this type was proven with distinct, steady values for ΔU as shown by all three data sets in figure 6.4. A noticeable, but unpredictable drift was observed between each set of data, with readings for each specific flow-rate changing by up to approximately 200μV between attempts.

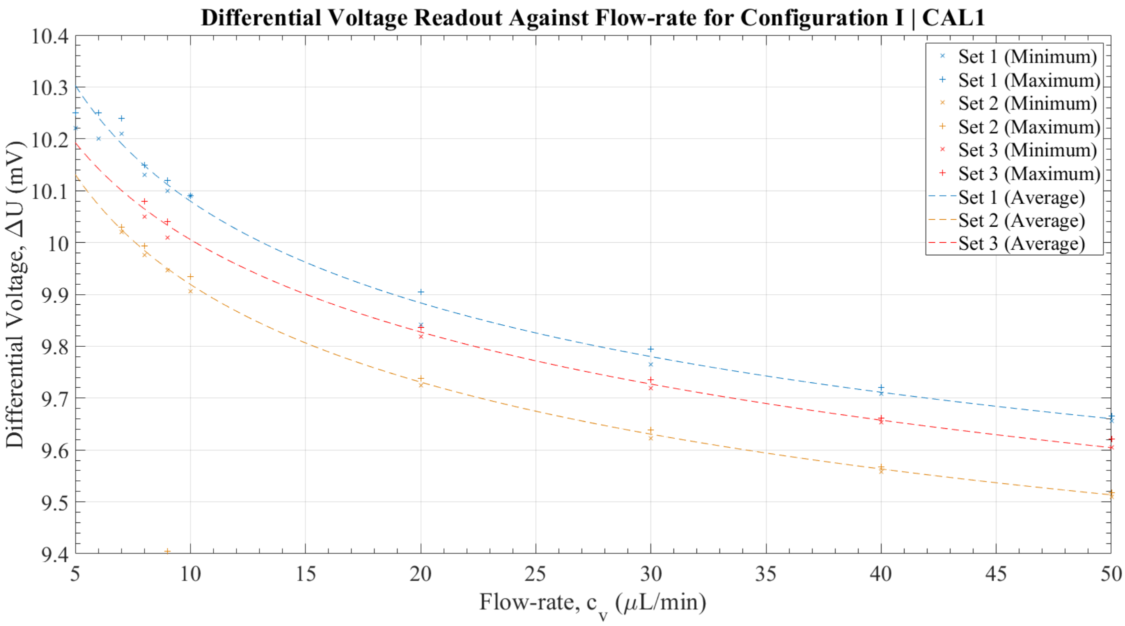

Figure 6.4: Voltage output with respect to flow-rate for the initial configuration.

The average value of ΔU for each dataset, as shown in figure 6.4, follows the trend of a two-term power function of the form $Ax^B + C$ with 95% confidence bounds. This implied that any detectable change between much higher flow-rates, for example those in excess of $c_v = 100\mu\text{l/min}$, would be far smaller than those at lower flow-rates like those measured here. This demonstrated a lack of sensitivity and prevented the design from being used for a broader range of applications. In addition to this, a primary disadvantage to be seen here was the fact that inconsistent voltage levels due to response drift prevented them from being characterised digitally for minimisation into a system capable of performing small-scale, rapid flow-rate analysis since this was one of the desirable outcomes of this project.

On the other hand it was noticed that, according to the data in figure 6.5, there was far more consistency in the *step* between each flow-rate measurement within a set of data. By taking the derivative of the datasets shown in figure 6.4, it became much clearer to see that there was a far closer relationship between the steps than there was between the voltage levels. Consequently, this design would have performed well in a calibrate-on-use setting, whereby the system could have been designed to determine the voltage levels with no flow-rate and a large flow-rate, using those as a basis to perform a more detailed analysis. However, this concept was not complementary to the problem being addressed in this account; flow-rate must be known in the first place in order for such a calibration design to function correctly in practice.

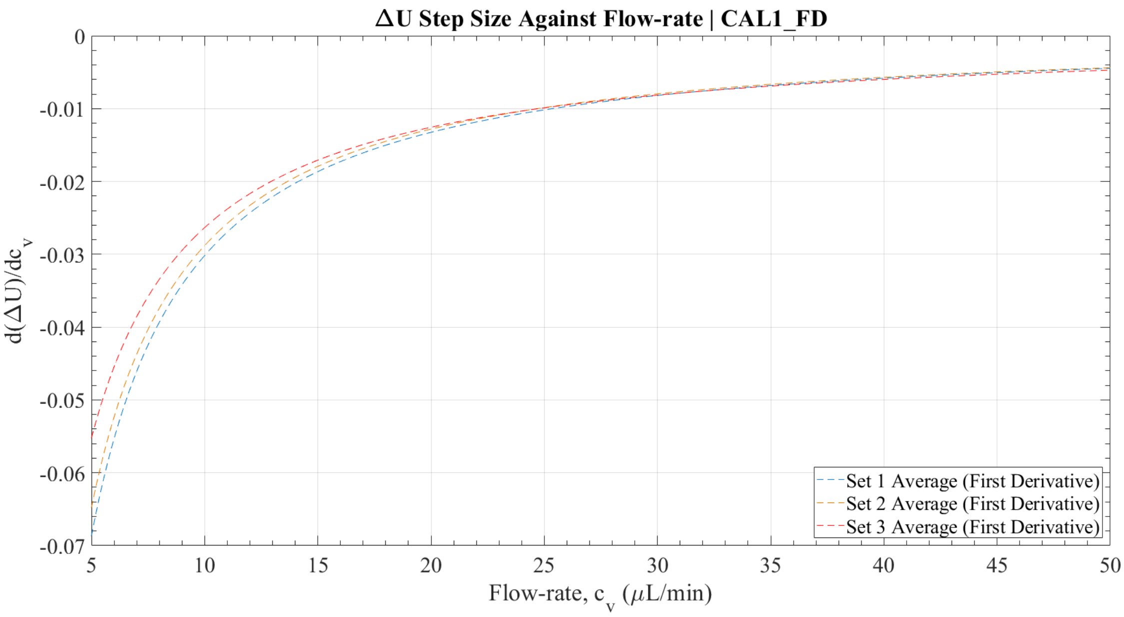

Figure 6.5: First derivative of the average data collected for a single heater configuration.

Upon looking at figure 6.1 on page 29, where data in figure 6.4 is shown with respect to time, it could be seen that the voltage readouts varied in their stability. It was observed how the stability of the low flow-rate measurements were in-fact questionable, with steady values for ΔU being held for flow-rates above $\sim 10\mu$l/min, but not consistently when below this value. It was to be noted that these effects were caused by a combination of the syringe pump and the syringe itself. Stepper-motors were the technology behind the operation of the *Fusion 400* syringe pump.

Essentially, a stepper motor increments about a given axis in very small steps creating a sudden 'jump' between x° of rotation and y° of rotation. When operating at higher flow-rates this transition can be far smoother, since the increments form a much less significant proportion of the total rotation per-unit time. At flow-rates below approximately 10μl/min however, these jumps became far more significant to the total rotation per-unit time, resulting in a pulsating flow-rate as opposed to a continuous one[1].

Furthermore, still in reference to figure 6.1, vibration-like patterns could be seen between 20 and 30μl/min on the first dataset as well as 8 and 9μl/min on the third. This was assumed to be, in part, down to the rubber bung catching periodically on the plastic syringe due to unbalanced friction forces at their interface. In practice, this effect occurs where the perimeter of the bung is held behind the center, before the force of the syringe pump causes it to jump forward suddenly, resulting in a momentary flow-rate variance. This fluctuation caused sensor data to be inconsistent and pulse further about the steady-state response for that given flow-rate. The effect of this, when coupled with the performance characteristics of the pump at these lower speeds, made getting stable measurements far more difficult.

[1] Based in-part on the opinions and experimentation of researchers at the *Centre for Hybrid Biodevices*

6.3 Multiple Heaters

On running more than one heating electrode in the channel, it could be seen how the response of the sensors differed greatly in comparison to what was expected. Instead of emphasising changes in ΔU with greater heat fluctuations, the system instead essentially flat-lined with a very limited response across all tested flow-rates. It was also noticeable how, in contrast to the trend found with the previous design, the value of ΔU *increased* with increasing flow-rate. This excludes dataset 2, which decreased with increasing flow-rate as was expected.

Despite this design offering very little along the lines of effective flow-rate measurement, what it did offer was an insight into the interactions between $u_h(t)$ and $u_s(t)$. Due to the flow-rate 'cloaking' effect of adding more heaters to the channel, it became both possible and reasonable to assume that the problem was a direct result of electrical interference from the much higher heater voltage; this time with $3\times$ the presence in the channel than before. The heaters' electric fields bent along the channel, towards that of the sensors, distorting and interfering with them in the process.

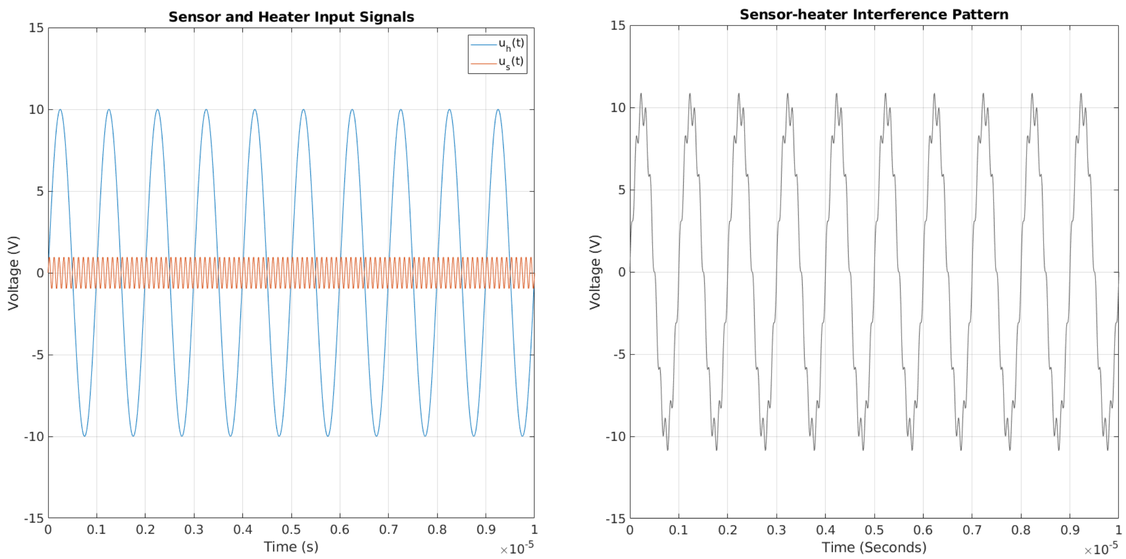

(a) Heater and sensor input signals.

(b) Heater and sensor signal interference.

Figure 6.6: The interference problem: An overview of the signal received at $u_x(t)$ or $u_y(t)$ when both $u_h(t)$ and $u_s(t)$ were driving the MFC.

This concept is best visualised in figure 6.6. On the left shows both $u_h(t)$ and $u_s(t)$, before they are input into the MFC and subsequently not interfering with one another. On the right is a representation of the either $u_x(t)$ or $u_y(t)$ when both the sensors and heaters were powered on. It was noticed how the heater signal, despite being emitted further down the channel from the sensors and separated from them by a grounding electrode, still remained largely overriding with the sensor signal becoming merely superimposed over the top of it. This gave access to potential problems, particularly with the PSD in-place on the LIA. Though such a device was capable of detecting these superimposed signals, the sudden and unpredictable shift regarding the constant constructive and destructive interference between them caused the phase ϕ_s of the sensor signal $u_s(t)$ to change.

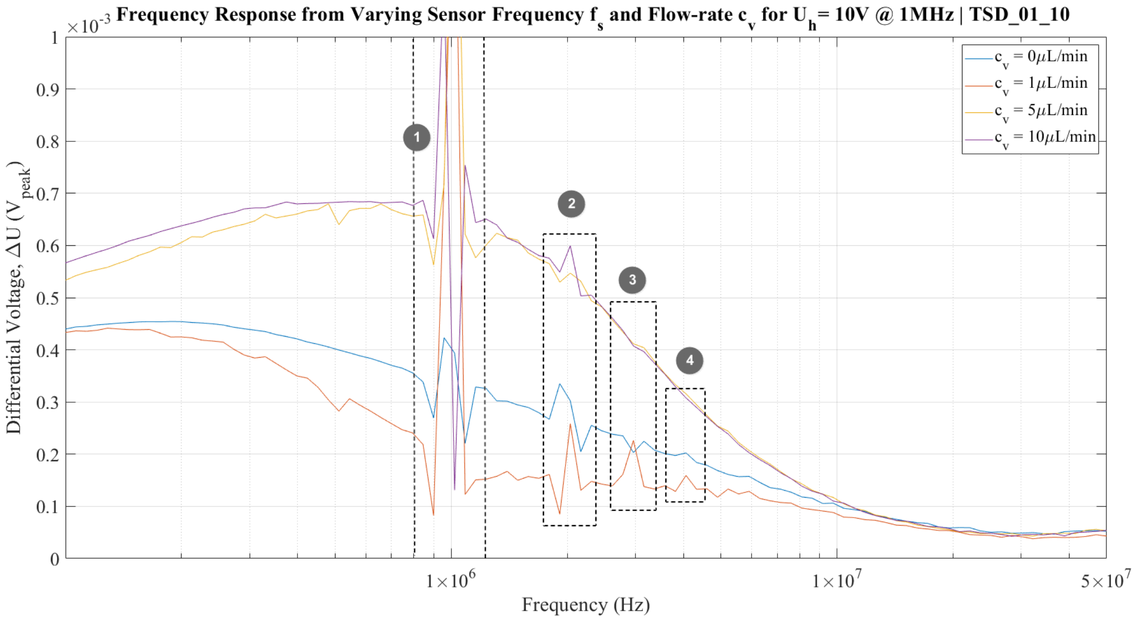

Figure 6.7: Frequency sweep implicating sensor-heater interference.

A further, brief experiment was carried out in order to see these supposed interference effects practically. Figure 6.7 shows data extracted for the differential sensor voltage ΔU on running a frequency sweep and varying the flow-rate per-sweep. Despite the sensors being most sensitive to flow-rate changes around $f_s = 1$MHz, as seen by the divergence of the four data plots, it was clear that both constructive and destructive interference were also causing sudden sharp spikes found at this frequency. Distortions like this do not necessarily imply interference, but in this case it was also possible to observe the second (2MHz), third (3MHz) and forth (4MHz) harmonics rippling along the length of the sweep; something that commonly occurs in systems with signal interference of this type.

6.4 The Use of Floating Sensors

Reverting back to the basic form of the initial configuration and applying passive sensors proved to be an effective design choice with far more consistent voltage levels seen here. In reference to figure 6.8, these levels were stretched out across voltages in the mV range as opposed to being in the hundreds of μV, like that seen with a single heater and active sensors. A slight drift was predominant within the range $10 \leq c_v \leq 30\mu$l/min but remained minor and still a significant improvement over the previous set of meaningful results in figure 6.4. Outside this range the data points had even stronger correlation and very little change could be seen between each dataset.

Drawing attention to figure 6.3 on page 31, it could be seen that the system was able to reach a steady-state response very quickly, with little tendency for readings to

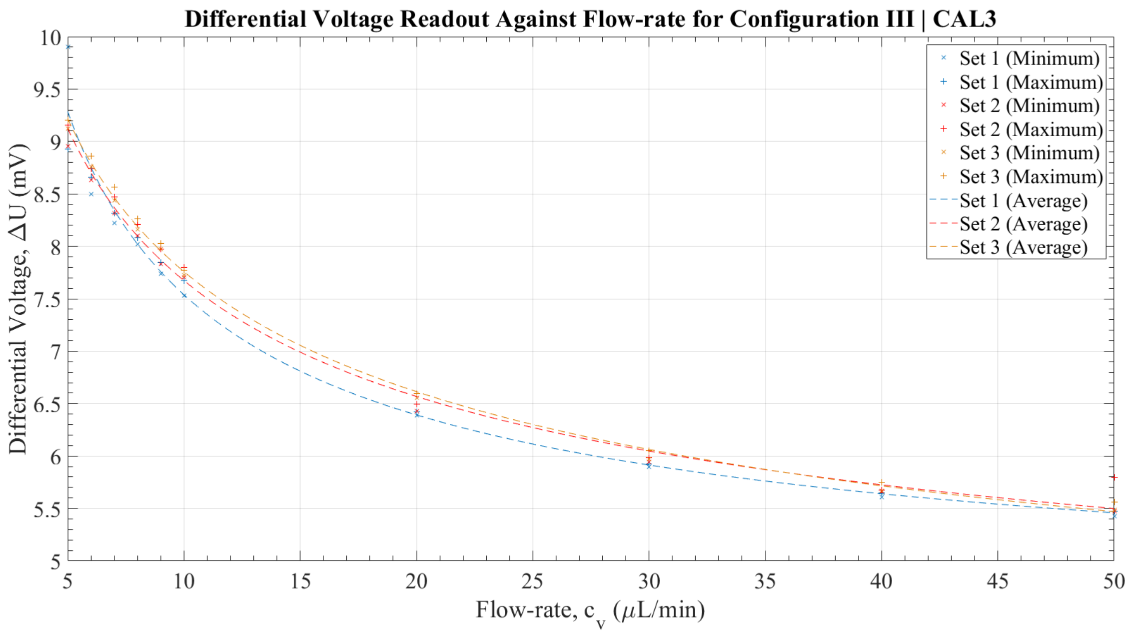

Figure 6.8: Voltage output against flow-rate for the third configuration.

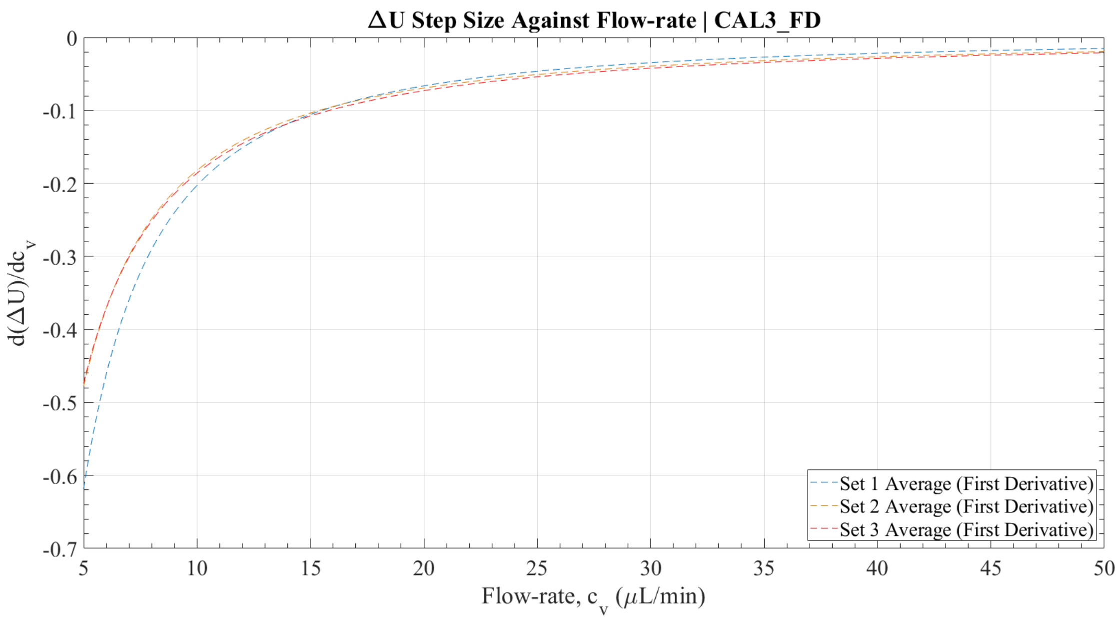

Figure 6.9: First derivative of the average data collected for a floating sensor configuration.

slowly ‘crawl’ up or down from a specific value. Furthermore, unlike preceding designs where no flow-rate was applied at all, the differential voltage appeared far more noisy than when there was. This implied the presence of electro-thermal currents generated by the heater causing static turbulence within the MFC.

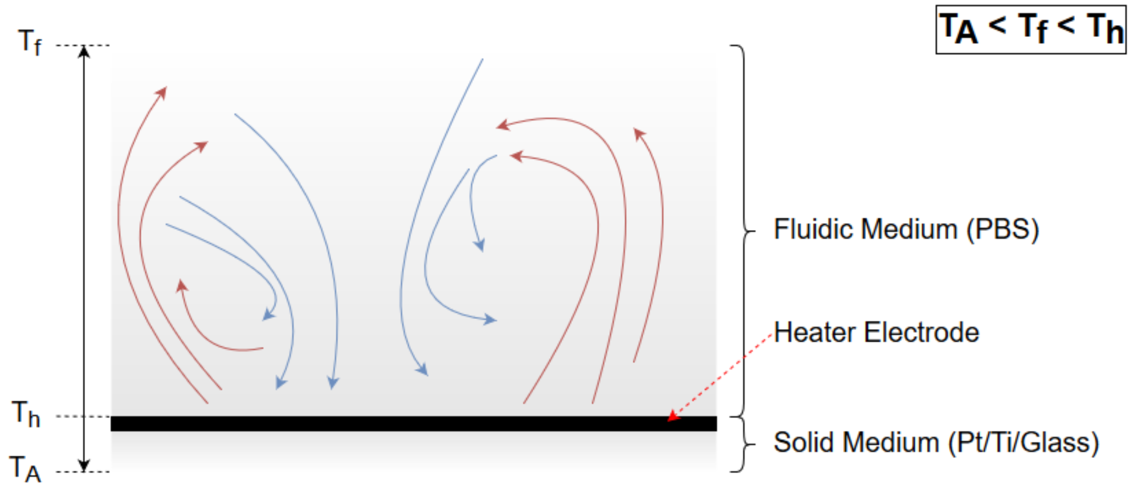

Figure 6.10: A visualisation of electro-thermal currents.

Essentially this meant that the PBS was being churned-up at the electrode-fluid interface through vortices created due to the thermal gradient across said fluid. The same thing occurs, and can be more readily seen, at the macro-scale when a kettle is switched on and actively heating the water. Liquids at a higher temperature have a tendency to rise against gravity, whilst the cooler liquid drops down in its place, a concept demonstrated in figure 6.10. These electro-thermal effects were, however, less dominant on the fluid’s movement at higher flow-rates. Not only was this observed in testing this design (figure 6.3, page 31), but it was also observed in the original design too (figure 6.1, page 29).

A noticeable, formidable jump could be seen repetitively on each dataset once the flow-rate had been discontinued; this same effect occurred in every design and on termination from any flow-rate, not just 50μl/min. Since the readouts are based on a differential between two sensors, $\Delta U = X - Y$, it was inevitable that there would have been some form of jump when the heater was switched on when the flow-rate was suddenly stopped. This occurred as a result of thermal redistribution, that is to say that the temperatures at both X and Y had to ‘realign’ themselves to establish a thermal equilibrium. For example, on referring back to figure 3.6, it was seen that under any forward flow-rate the heat energy dissipated from the heater was ‘pushed’ down the channel towards Y. When the flow was stopped however, the temperature at Y would have increased briefly as the flow-rate slows down, then dropped back down towards equilibrium, whilst the temperature at X rose very slowly until that of the pair became roughly equal once again.

Relating this to the theory outlined in sections 3.4.2 and 5.2, the voltage $u_y(t)$ would have suddenly dropped and then increased, whilst $u_x(t)$ would have slowly dropped. Given this information, ΔU would have suddenly increased, and then dropped to a constant level; facts supported by the data shown in both figures 6.2 and 6.3.

On relation of the consistency of this design with the LOC device ideology, on a similar note to that mentioned in section 6.2, this peak was applicable in a calibration setting. Used in coupling with the step response between flow-rates, shown in figure 6.9, a difference between the voltage at a known 0μl/min and one of a non-zero flow-rate could be observable and thus easily reportable to an external system. Predictable voltage levels offer a far greater probability of using digital electronics to reference these back to a given flow-rate. With the drift minimised, though not completely removed, calibration need-not be done on the submission of each new sample, but instead checked through brief testing at given intervals when required.

Chapter 7

Summary and Conclusions

7.1 In Summary

In collation of all the data gathered for this project, as well as the many observations made during experimentation, a rudimentary 'roadmap' was created outlining how various design decisions impacted the two most important factors for systems of this type; *stability* and *sensitivity*.

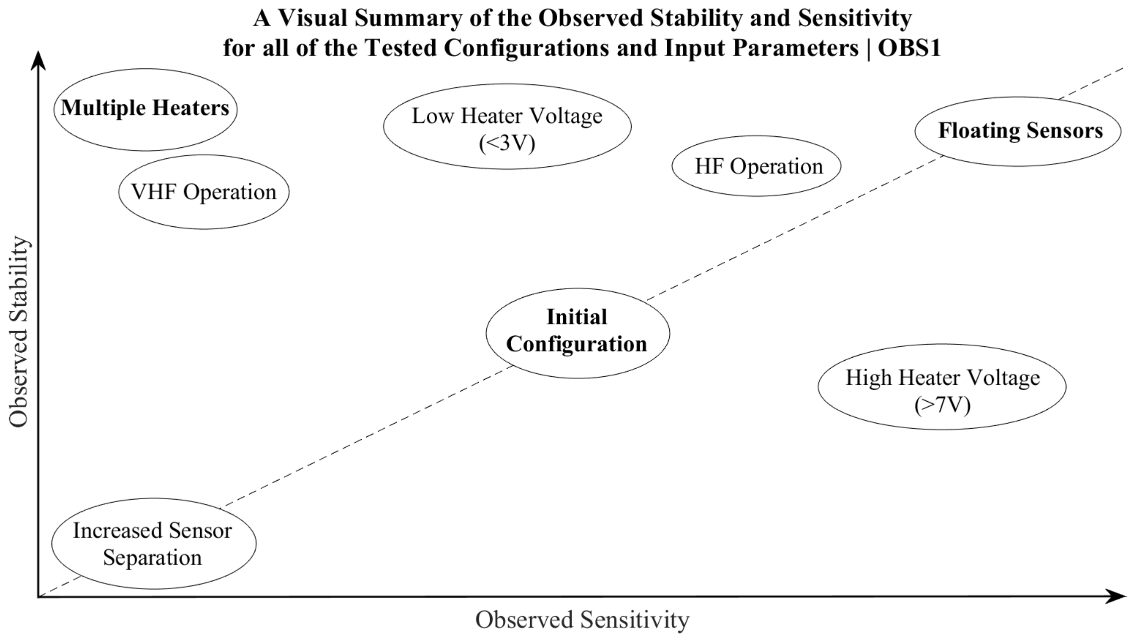

Figure 7.1: A graphical overview of the various design implications: Combining the results and analyses for each configuration, as well as the different input parameters provided to them, taken with respect to the performance of the initial configuration as tested using the methodology described in section 5.1.

Figure 7.1 is inclusive of a wide variety of performance-altering parameters, whether-or-not they were beneficial. Firstly, the initial design incorporating a single heater was used as a reference point. With modest performance, but still encountering issues of its own, this design offered moderate sensitivity for detecting many different flow-rates, but poor stability at those particularly low. Despite its poor sensitivity the design with three heaters was stable whilst it was operating, at the same time the design with floating sensors proved itself to include the best of both worlds.

Certain other factors were tested when it came to improving performance. For example, the effects of varying the heater voltage $u_h(t)$. Due to project and resource constraints, this could not be documented specifically but has been outlined in figure 7.1. Lower heater voltages, particularly those below 3V, provided greater stability to the to the measurements but lacked sufficient sensitivity. This is to say that, as less heat energy was being placed into the channel, far lower rates of flow were needed to 'flush away' the generated heat, leaving both sensors detecting near-identical temperatures and no difference could be observed. On the other hand using high heater voltages, as with the 10V used throughout this project, often caused unpredictable drifts in sensor outputs but offered far more sensitivity to changes even at much higher flow-rates.

Sensor frequency f_s, where applicable, was also a factor that affected sensitivity of measurement. When very high frequency (VHF)[1] signals were applied to the sensor electrodes, regardless of their voltage, the response of the system became minimal. This was similar to the observations made when using multiple heaters. Conversely, high frequency (HF)[2] signals and just below worked far better and would be recommended for active sensor implementations.

Overall, it could be clearly seen in both theory and practice that the use of passive sensor electrodes for micro-thermal flow-rate detection was far more plausible than the others explored here. Being the simplest design, it also boasted the lowest power consumption - a very important quality for micro-scale systems, where high power density becomes a substantial factor in their design.

7.2 Future Development

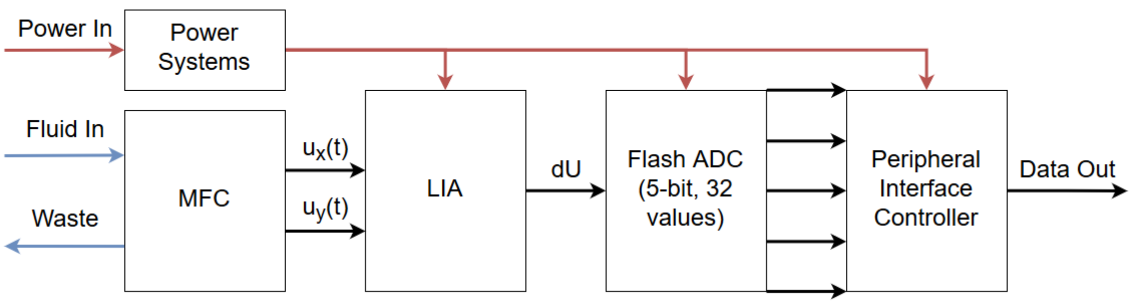

Figure 7.2: An example LOC integrated system setup.

The research presented here forms only the basis for a sensor of this type. Further work needed to be carried out before a system matching the description of that in the introduction could be designed. Two of the core problems that were yet to be

[1] Defined as frequencies between 30MHz and 300MHz [28].
[2] Defined as frequencies between 3MHz and 30MHz [28].

faced along with a rough system diagram to aid with the descriptions are outlined briefly here.

Results from the experimentation carried out as described in both chapters 4 and 5 required the used of a LIA. This particular model, though indicative of many others, was bulky, powerful and not-so-portable making it a far-fetched choice for a supposedly miniature system. Before the system can be scaled-down, this piece of measurement hardware needed be shrunk down too.

Even with a LIA analysing the signals taken directly from the MFC, the value of ΔU remained analogue and incomprehensible by any form of computational processing subsystem. Sticking with the LOC ideology, any flow-rate analysis would need to be performed on-chip, therefore a form of analogue-to-digital conversion would need to take place here. A flash ADC design would offer a rapid and accurate means to achieve this, if designed with levels correlating to those shown in figure 6.8.

With both of these two problems solved, it would be possible to make a micro-scale flow-rate *regulator*, whereby flow-rates can not only be measured, but also controlled. This would have useful applications in microchip liquid cooling systems, micro-scale fluid handling and biological sample handling.

7.3 Final Thoughts

The success of this project was highly dependant on the careful planning of lab-based experimentation, background reading and theoretical analysis. In an effort to ensure the project as-a-whole was completed to a high standard, detailed project planning and management took place where weekly goals and consistent milestones were laid-out. A project timeline, taking the form of a Gantt chart, was designed to provide ambitious targets over a reasonable time-frame. Despite several changes to this timeline, the overall aim of the project, as described in the introduction and project brief (appendix A), was met with many different ideas and designs being conceptualised, eventually yielding results for the project.

Despite a slow start, consistent progress was made on access to the *Center for Hybrid Biodevices* with only a few tasks having minor set-backs. As shown between appendices C and D, very little was changed between the progress report in December 2017 and the final, with exception to some minor experimental changes. Regular meetings with the project supervisor proved very beneficial, often leading to sudden epiphanies regarding data that would not have occurred otherwise due to the subject-span of this project. On this note, further work could have been done at the earlier stages, when progress was slower, to understand concepts inherently unknown at the time.

In an attempt to prepare for the unexpected, a brief risk assessment (appendix B) was drawn-up and auxiliary goals were outlined. Provided the project became unachievable, under the supervisor's instruction and advice, the project brief would have been amended and the direction of the project changed towards a more 'achievable goal'; this was never required nor sought-after, but left in-place as a form of risk management and damage reduction.

In conclusion, *Micro-thermal Flow-rate Detection for Lab-on-a-chip Technologies* proved to be endlessly challenging, engaging and yet highly enjoyable. With new research demonstrating exciting new concepts for flow-rate sensing at the microscopic scale, this project leaves behind many avenues for the continued research and development in such technologies in the future.

Bibliography

[1] J. T. W. Kuo, L. Yu, and E. Meng, “Micromachined thermal flow sensors—a review,” *Micromachines*, vol. 3, no. 4, pp. 550–573, jul 2012.

[2] H. Berthet, J. Jundt, J. Durivault, B. Mercier, and D. Angelescu, “Time-of-flight thermal flowrate sensor for lab-on-chip applications,” *Lab Chip*, vol. 11, no. 2, pp. 215–223, 2011.

[3] P. Roy, M. R. Patra, H. Rahaman, and P. Dasgupta, “An intelligent biochip system for diagnostic process flow based integration of combined detection analyzer,” in *2013 International Symposium on Electronic System Design*. IEEE, dec 2013.

[4] P. Tabeling, *Introduction to Microfluidics*. OXFORD UNIV PR, 2010.

[5] S. C. Terry, “A gas chromatography system fabricated on a silicon wafer using integrated circuit technology,” phdthesis, Stanford University, 1975.

[6] F. Shaun, H. Regina, F. Marty, E. Nefzaoui, T. Bourouina, and W. Cesar, “Design of micro-fabricated thermal flow-rate sensor for water network monitoring,” in *2017 Symposium on Design, Test, Integration and Packaging of MEMS/MOEMS (DTIP)*. IEEE, may 2017.

[7] F. Shaun, E. Nefzaoui, H. Regina, W. Cesar, F. Marty, M. Capochichi-Gnambodoe, P. Poulichet, P. Basset, F. Peressuti, S. Sarkar, and T. Bourouina, “On the co-integration of a thermo-resistive flow-rate sensor in a multi-parameter sensing chip for water network monitoring,” in *2017 19th International Conference on Solid-State Sensors, Actuators and Microsystems (TRANSDUCERS)*. IEEE, jun 2017.

[8] J. E. Kong, Q. Wei, D. Tseng, J. Zhang, E. Pan, M. Lewinski, O. B. Garner, A. Ozcan, and D. D. Carlo, “Highly stable and sensitive nucleic acid amplification and cell-phone-based readout,” *ACS Nano*, vol. 11, no. 3, pp. 2934–2943, mar 2017.

[9] F. Tay, W. Choong, H. Liu, and G. Xu, “An intelligent micro-fluidic system for drug delivery,” in *Proceedings of IEEE International Conference on Industrial Technology 2000 (IEEE Cat. No.00TH8482)*. Jaico Publishing House, 2000.

[10] K.-Y. Chen, K.-E. Chen, and K. Wang, “A flexible evaporation micropump with precision flow rate control for micro-fluidic systems,” in *2012 7th IEEE*

International Conference on Nano/Micro Engineered and Molecular Systems (NEMS). IEEE, mar 2012.

[11] S. Sarasu and K. Rama, "Design and development of organ on chip using microfluidic technology for simulation," in *2013 International Conference on Optical Imaging Sensor and Security (ICOSS).* IEEE, jul 2013.

[12] M. Ibrahim and K. Chakrabarty, "Digital-microfluidic biochips for quantitative analysis: Bridging the gap between microfluidics and microbiology," in *Design, Automation & Test in Europe Conference & Exhibition (DATE), 2017.* IEEE, mar 2017.

[13] V. Shukla, F. Hussin, N. Hamid, and N. Z. Ali, "Advances in testing techniques for digital microfluidic biochips," *Sensors*, vol. 17, no. 8, p. 1719, jul 2017.

[14] S. Misra, W. G. John, G. Alberti, J. H. Barth, E. English, J. Valabhji, and N. Oliver, "The use of POCT HbA1c devices in the NHS Diabetes Prevention Programme: Recommendations from an expert working group commissioned by NHS England," Jul. 2016.

[15] C. P. Price, "Regular review: Point of care testing," *BMJ*, vol. 322, no. 7297, pp. 1285–1288, may 2001.

[16] D. R. Reyes, D. Iossifidis, P.-A. Auroux, and A. Manz, "Micro total analysis systems. 1. introduction, theory, and technology," *Analytical Chemistry*, vol. 74, no. 12, pp. 2623–2636, jun 2002.

[17] P.-A. Auroux, D. Iossifidis, D. R. Reyes, and A. Manz, "Micro total analysis systems. 2. analytical standard operations and applications," *Analytical Chemistry*, vol. 74, no. 12, pp. 2637–2652, jun 2002.

[18] T. Karayiannis and M. Collins, *3rd Micro and Nano Flow Conference 2011.* Brunel University Press, 2011.

[19] H. Fujita, T. Ohhashi, M. Asakura, M. Yamada, and K. Watanabe, "A thermistor anemometer for low-flow-rate measurements," *IEEE Transactions on Instrumentation and Measurement*, vol. 44, no. 3, pp. 779–782, jun 1994.

[20] A.-J. Maki, A. Kontunen, T. Ryynanen, J. Verho, J. Kreutzer, J. Lekkala, and P. Kallio, "Design and simulation of a thermal flow sensor for gravity-driven microfluidic applications," in *2016 IEEE 11th Annual International Conference on Nano/Micro Engineered and Molecular Systems (NEMS).* IEEE, apr 2016.

[21] S. Cerimovic, F. Keplinger, R. Beigelbeck, A. Jachimowicz, H. Antlinger, and B. Jakoby, "Monitoring the glycerol concentration in aqueous glycerol solutions using a micromachined flow sensor," in *2014 Microelectronic Systems Symposium (MESS).* IEEE, may 2014.

[22] G. Comte-Bellot, "Hot-wire anemometry," *Annual Review of Fluid Mechanics*, vol. 8, no. 1, pp. 209–231, jan 1976.

[23] C. K. Harnett, B. P. Mosier, P. F. Caton, B. Weidenman, and R. W. Crocker, "Conductivity of tim-of-flight flow sensor for sub-microliter/minute flow rates,"

in *7th International Conference on Miniaturized Chemical and Biochemical Analysis Systems.* IEEE, 2003.

[24] D. Spencer, "Advanced Microfluidic Impedance Cytometry for Point of Care Analysis," phdthesis, University of Southampton, Sep. 2013.

[25] C. J. Seeton, "Viscosity–temperature correlation for liquids," *Tribology Letters*, vol. 22, no. 1, pp. 67–78, apr 2006.

[26] J. J. Barron and C. Ashton, "The effect of temperature on conductivity measurement," Apr. 2011.

[27] A. Gonzalez, A. Ramos, H. Morgan, N. G. Green, and A. Castellanos, "Electrothermal flows generated by alternating and rotating electric fields in microsystems," *Fluid Mechanics*, vol. 564, pp. 415–433, 2006.

[28] IEEE Aerospace and Electronic Systems Society, "IEEE standard letter designations for radar-frequency bands," *IEEE Std 521-2002 (Revision of IEEE Std 521-1984)*, 2003.

Appendices

A Project Brief

The ability to observe and analyse the flow of a gas or liquid within a medium of varying complexity has distinct applications ranging from the monitoring of fuel flow and quality through a combustion engine to the sensitive observation and subsequent control of a clean-room environment under strict sterile conditions. The uses of such technologies can be further expanded into the realm of lab-on-a-chip devices to perform tasks such as monitoring the flow of blood cells as well as analysing them for potential problems.

Thermal diffusion occurs along a thermal gradient from an area of higher temperature to that of a lower temperature. This process occurs throughout any type of medium, be it a solid, liquid or gas. By analysing the diffusion pattern of a burst of heat energy, we can identify many useful properties of that medium. I proposed the use of a micro-thermal flow sensor constructed within a LOC device to detect the flow-rate of saline under varying conditions, showing both how baseline measurements vary and thus counteracting their negative effects on the reading's accuracy. By applying a voltage across the conductive fluid using a pair of parallel electrodes, a current will flow through the saline and it could therefore effectively be seen as a resistor. As with any resistance, energy is dissipated in a variety of ways; heat being one of these. Two more electrode pairs, one upstream from the heater and another downstream from it, enabled a difference in signal to be analysed; any difference is down to differing fluid properties at those electrodes. This form of flow-rate sensor is known as calorimetric and, using it, an investigation on how temperature effects the conductivity of the fluid could be carried out.

The primary goal of this project is to be able to identify and analyse the flow-rate of saline through a micro-machined fluidic chip whilst detailing how the variation of fluid temperature affects conductivity properties. On top of this, an important area of consideration throughout this project is to develop a system that is capable of processing such a fluid without the need for vast, complex and expensive equipment. This would be of great benefit across multiple disciplines such as Chemistry, Biology, Medicine and Engineering, all of which typically use such equipment to perform measurements at this scale.

B Risk Assessment

Description	Loss	Probability	Risk	Controllable?
Access to the bio-lab is restricted through uncontrollable and/or unforeseeable means.	4	3	12	No
Injury within the laboratory environment as a result of diverging attention or incompetence.	2	2	4	Yes
Damage or destruction to laboratory equipment as a result of diverging attention or incompetence.	5	1	5	Yes
Damage to microchip as a result of experimental error.	3	3	9	Yes
Loss of data due to hardware failure.	5	1	5	Yes
Delays due to personal illness.	2	2	4	No
Lab results recorded incorrectly due to equipment calibration error.	4	3	12	Yes
Unrecoverable project issue(s) cause preset goals to become unrealistic.	5	1	5	No
Long manufacturing lead-time causes significant delays in the progression of the project.	4	1	4	No
Project delays as a result of late component manufacture/ordering.	4	1	4	Yes
Failure to achieve project goals within the time allotted on the project timeline.	3	3	9	Yes

Revision 3, 01/04/2018

C Interim Project Timeline

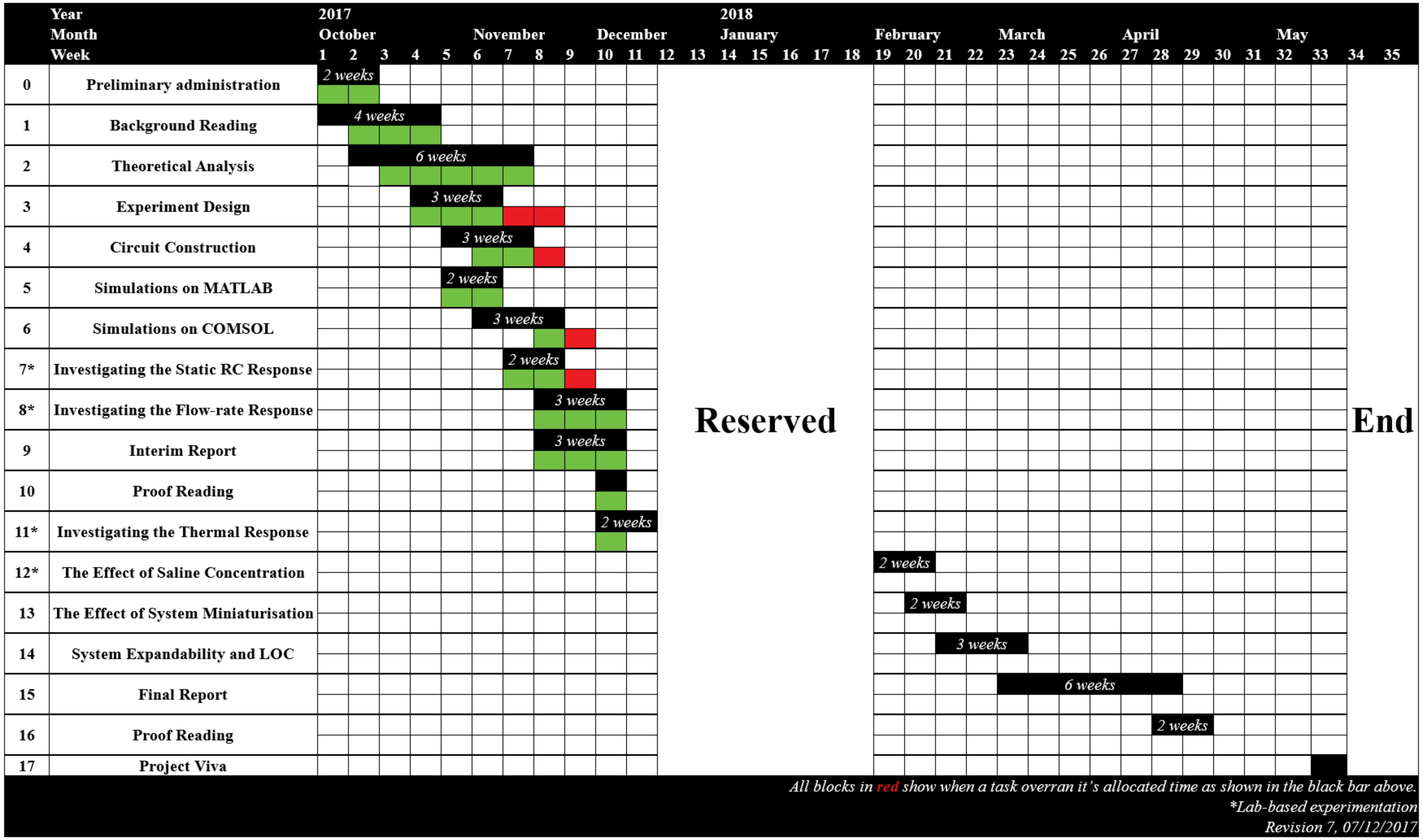

D Final Project Timeline

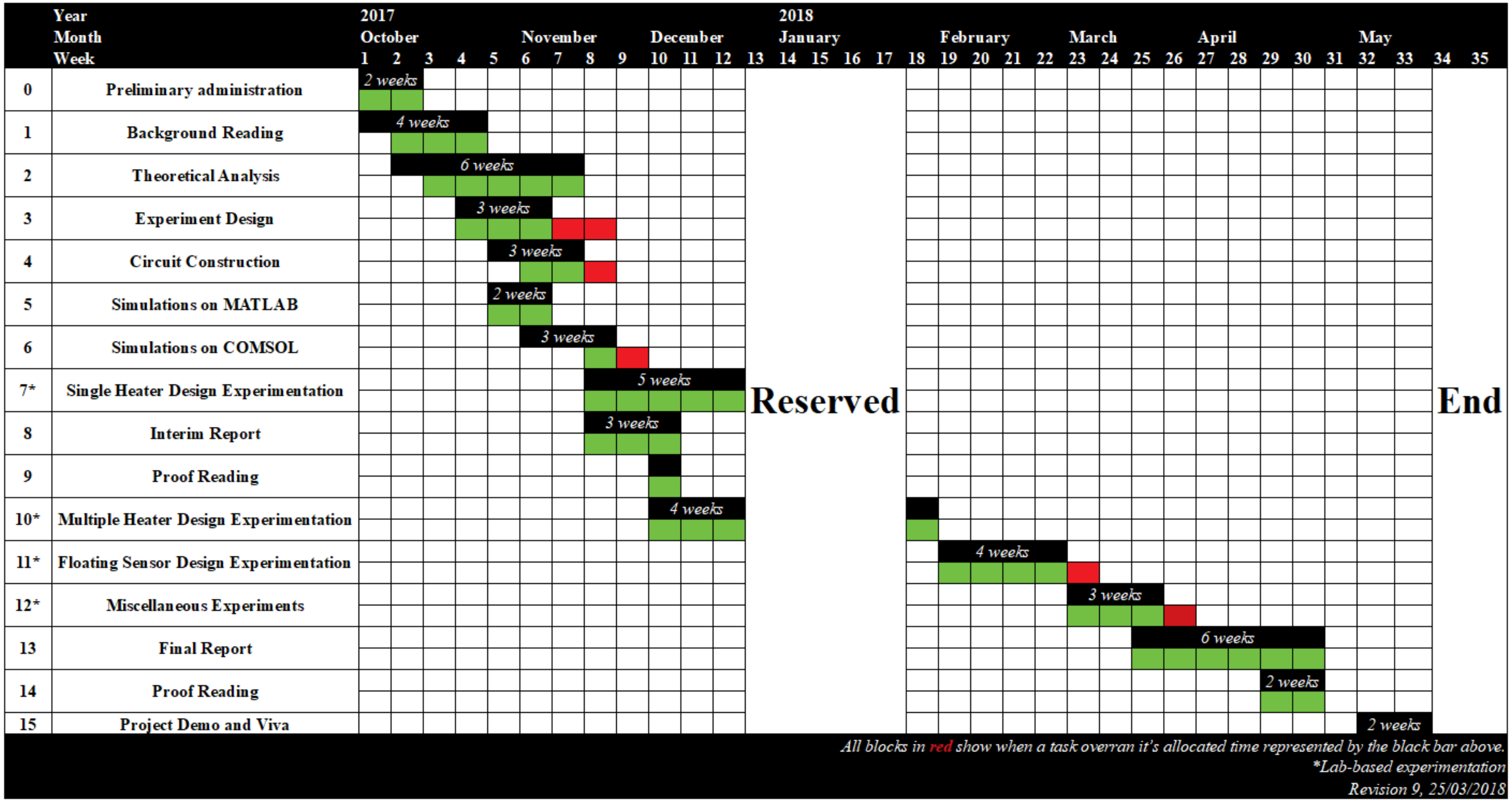

E Volumetric Flow-rate to Linear Speed

Volumetric flow-rate c_V, throughout this account, is measured in μl/min. Simulation packages can require this value to be represented as a linear speed c_L in m/s. A conversion can be performed by considering the dimensions of the micro-fluidic chips as outlined in section 2.3, more specifically the volume V between the electrode plates. Firstly, c_V needed to be expressed in terms of meters cubed per second rather than litres, this is done with the following relation:

$$1\mu\text{L/min} \rightarrow 10^9\mu\text{m}^3/\text{min} \rightarrow \frac{10^9}{60}\mu\text{m}^3/\text{s} \rightarrow \frac{10^{-9}}{60}\text{m}^3/\text{s}$$

Where $\frac{10^{-9}}{60}$ is the conversion factor in this case. The number of times the volume enclosed by the electrode plates is filled per unit time V_m can be said to be:

$$V_m = \frac{10^{-9}}{60V}c_V$$

This gives a linear speed c_L in meters per second:

$$\begin{aligned} c_L &= V_m L \\ &= \frac{10^{-9}L}{60V}c_V \end{aligned}$$

IMPORTANT: Since the above equation is dependant on volume, the values outlined in the table below are only valid when considering the speed **inside** the MFCs channel as described in section 2.3.

Flow-rate c_V (μl/min)	**Speed c_L (m/s)**
1	0.0104
2	0.0208
3	0.0313
4	0.0417
5	0.0521
6	0.0625
7	0.0729
8	0.0833
9	0.0938
10	0.1040
20	0.2080
30	0.3125
40	0.4170
50	0.5210
60	0.6250
70	0.7290
80	0.8330
90	0.9380
100	1.0400

F Micro-fluidic Velocity Profile

In attention to fluid dynamics, it could be seen that the movement of a fluid through an enclosed medium, such as a pipe, causes an arc-like pattern at the head of that fluid. This pattern is due to viscous drag along the fluid-solid interface causing the fluid motion along it to be zero. This causes parallel layers to be formed with different velocities within the liquid, increasing to a maximum at the cross-sectional center of the fluid in motion. Essentially, each layer slides across the top of one-another with their own velocity; a rudimentary illustration of this was seen in figure 3.1.

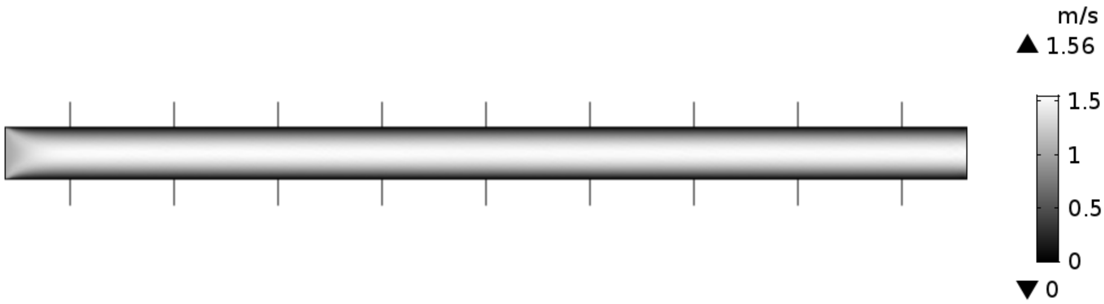

MFC internal fluid velocity profile for a flow-rate of 150μl/min.

The effects of this non-linearity are more noticeable at smaller scales; at the micro-scale, this needed to be considered. Through further simulations on *COMSOL Multiphysics*, a 2-D velocity profile for deionised water flowing through the channel was obtained. This can be seen in the figure above. This viscous drag had already been considered when running the thermal diffusion simulations shown on page 14.

G Heat Dissipation for Three Heaters

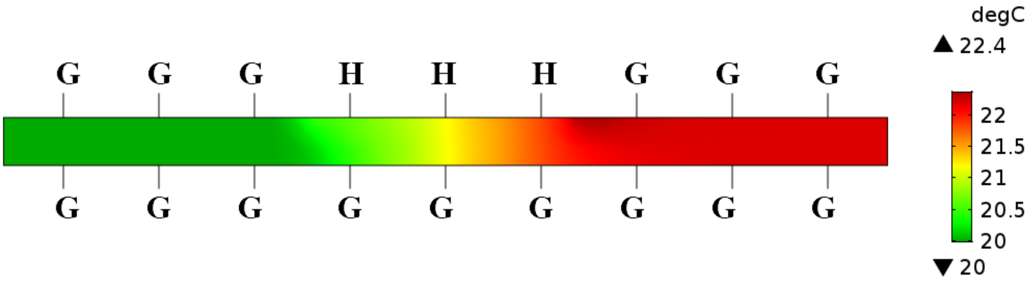

Flow-rate = 5μl/min.

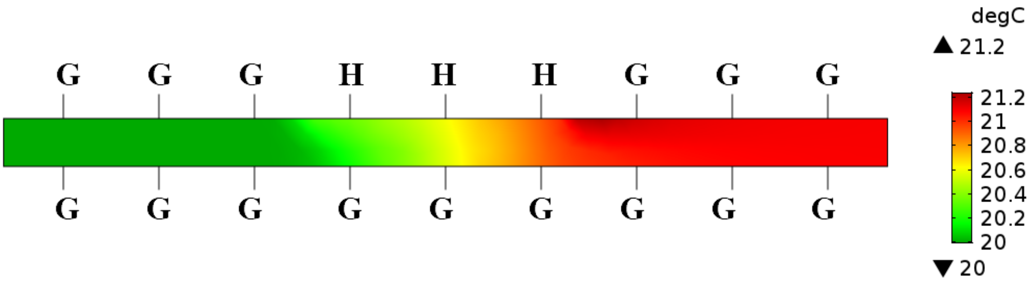

Flow-rate = 10μl/min.

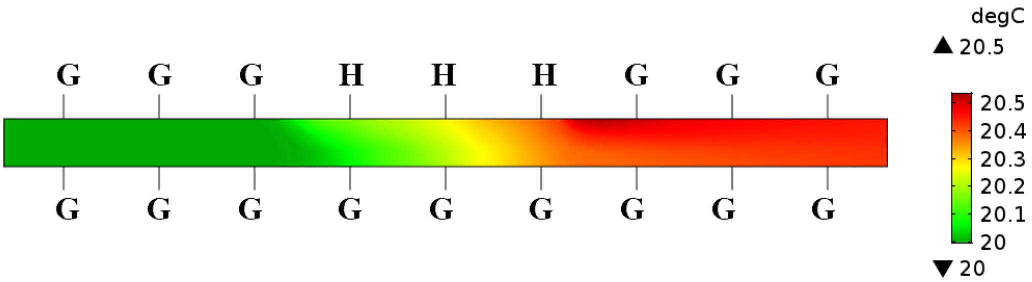

Flow-rate = 25μl/min.

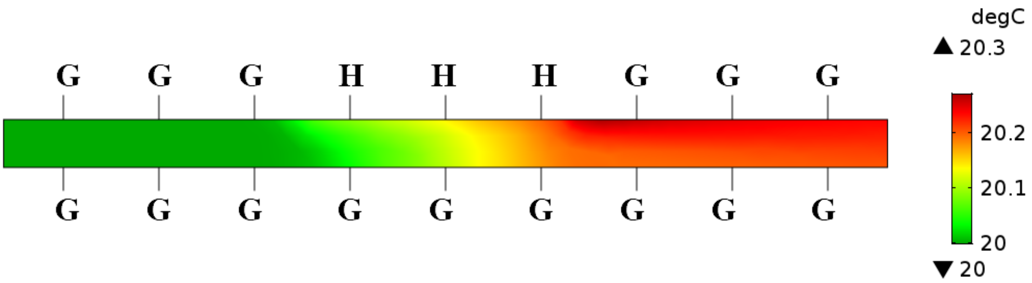

Flow-rate = 50μl/min.